Phase field fracture in elasto-plastic solids: Considering complex loading history for crushing simulations

Cunyi Li [a], Jianguang Fang [a,*], Na Qiu [b], Chi Wu [c], Grant Steven [c], Qing Li [c]

[a] School of Civil and Environmental Engineering, University of Technology Sydney, Sydney, NSW 2007, Australia
[b] Mechanical and Electrical Engineering College, Hainan University, Haikou 570228, China
[c] School of Aerospace, Mechanical and Mechatronic Engineering, The University of Sydney, Sydney, NSW 2006, Australia

ARTICLE INFO

ABSTRACT

Phase field models have gained growing popularity in fracture analysis. However, phase field modelling remains lacking for complex real-life applications such as structural crushing analyses to date. The novelty of this study is to propose an explicit phase field modelling framework considering complex loading history to predict the crushing behaviour of additively manufactured metallic structures. First, the explicit phase field model is formulated by considering stress state dependent fracture initiations with non-proportional loading. Then, five types of material specimens with a wide range of stress states are experimentally tested to calibrate material parameters for additively manufactured 316L steel and Ti-6Al-4V titanium. Last, the square tubes are 3D-printed and tested under three-point bending and axial compression to demonstrate the capacity of the proposed model. The modelling results unveil that the crushing behaviour of both materials could be properly reproduced in terms of force-displacement curves and crack paths. Finally, the fracture mechanism of crushing deformation is analysed. For the three-point bending of Ti-6Al-4V tubes, cracks are mainly induced by the medium stress triaxiality tension and shear loading. For the axial compression of 316L tubes, the stress states of critical elements are relatively diverse yet slightly concentrated at the shear, compression-shear, and high stress triaxiality tension regions. Remarkably, non-proportional loading is significant in crushing deformation as a material point may experience a significant change in stress state with loading. By considering a non-proportional loading dependent threshold, the proposed phase field model can predict the crushing behaviour of structures even when the fracture initiations do not locate on the fracture locus. This study provides an effective explicit phase field framework featured with an insightful fracture mechanism for quasi-static crushing of additively manufactured metallic materials.

1. Introduction

The phase field fracture model has gained significant usage due to its superior capability for capturing intricate fracture phenomena, including crack nucleation, propagation, branching, and merging [1]. Phase field originated from variational principles by Francfort and Marigo [2] and was subsequently implemented numerically by Bourdin et al. [3]. Over the past two decades, the phase field method has been extensively explored in various fracture domains, encompassing brittle fracture [4,5], ductile fracture [6,7], dynamic fracture [8,9], non-deterministic fracture [10,11], and multi-field fracture [12,13].

Despite the above-mentioned application scenarios, to the authors' best knowledge, the phase field model has not been used in the context

of crushing, which commonly involve large deformation and rather complex mechanical behaviour [14,15]. The prediction of crushing behaviour is of primary importance in analysing and optimising the crashworthiness and energy absorption of materials and structures. However, fractures are often neglected in the analysis of crushing behaviour [16], which is partially due to the fact that conventional metallic materials such as mild steels and low-strength aluminium alloys exhibit fairly high ductility [17,18]. However, the ductility of emerging high-strength steels may be compromised by their high strength [19]. Liu et al. [19] applied an extended modified Bai-Wierzbicki fracture model to predict the crack formation of progressive folding of square tubes for dual-phase steel sheets.

With the rapid advances in additive manufacturing technologies, 3D-

---

printed metals have been extensively studied and often tend to exhibit worse ductility [20]. For instance, the fracture strain of the 3D-printed Ti-6Al-4V was only around 1/10 of its mill-annealed counterpart under tensile and shearing loads [20]. For this reason, it would be indispensable to simulate fracture for analysing the crushing behaviour of these less ductile materials. In this regard, Li et al. [21] adopted the Hosford-Coulomb fracture model for analysing crushing behaviour of shell lattices made of Laser Powder Bed Fusion (LPBF) 316L steel. Qiu et al. [22] applied the Johnson-Cook damage model to simulate fracture behaviour of three-dimensional functionally graded structures.

Nevertheless, local damage models [23,24] were used in these abovementioned studies, which may lead to strong mesh dependency [25] due to there being no unique solution for strain localisation [26]. In practice, consistent element sizes at the cracking region were employed for both material and structural samples to avoid the negative influence of mesh size [19]. Also, a characteristic length dependent on element size is introduced to alleviate the mesh dependency [27]. In this aspect, the phase field fracture model may achieve better mesh objectivity [7,28] due to its similarity to gradient damage models [29,30].

Furthermore, an implicit solver might not be suitable for crushing simulation due to frequently changing contact conditions, which requires more iterations per increment and may even lead to divergence [31,32]. Also, local instabilities pose significant challenges for convergence [31,32]. In contrast, an explicit solver would be an attractive alternative for crushing simulation due to its capability to overcome the above numerical issues [33,34]. In the community of phase field modelling, Ren et al. [35] proposed an explicit phase field model for dynamic brittle fracture. Chu et al. [9] applied an explicit phase field model to elucidate the fracture mechanism behind the transition from brittle to ductile failure modes in metallic materials. Ziaei-Rad and Shen [36] developed a parallelised phase field framework to reduce computational cost for large-scale analysis. Mandal et al. [37] presented a length scale insensitive phase field model for brittle fracture in anisotropic hyperelastic solid. Zhang et al. [38] proposed an explicit phase field total Lagrangian material point method to simulate dynamic fracture of hyperelastic solids. Zhang and Tabiei [39] developed a staggered scheme for the explicit phase field method, where the phase field was solved every certain time step to lower computational cost. Wang et al. [40] proposed a thermo-elastic coupled phase field model applicable to quasi-static and dynamic crack scenarios. Recently, more explicit phase field models have been developed for quasi-static loading. For example, Hu et al. [41] compared the implicit and explicit phase field models for quasi-static problems. They suggested that when using an explicit solver, the kinetic and viscous energies should be sufficiently small compared to the external work for quasi-static loading [41]. Sahin et al. [42] proposed an explicit phase field model enriched by a nonlocal operator for crack propagation under quasi-static loading.

Nevertheless, the aforementioned explicit phase field models have mainly focused on brittle fracture where damage initiates at an early stage of loading. In the context of ductile fracture, Wang et al. [43,44] studied adiabatic shear band via thermos-elastic-plastic phase field model, where both damage and thermal softening were considered. Hu et al. [45] coupled the phase field method with the material point method to simulate large deformation elastoplastic failure for fully saturated porous media. However, there should be a fracture threshold to reproduce experimental results [12,46]. Further, the fracture threshold should be stress state dependent for different fracture modes [47,48] and multi-axial loading [49,50]. Due to varying stress states in the loading process, it is necessary to consider non-proportional loading for the threshold [48,51]. In this regard, Papasidero et al. [52] discovered that pre-compression augmented the fracture strain for shear, whereas pre-tension diminished the fracture strain for shear. Zhuang et al. [53] revealed that for compression-torsion loading, pre-compression contributed a minimal contribution to damage accumulation due to the cut-off value for stress triaxiality, thereby delaying the initiation of fracture. Benzerga et al. [54] found that the fracture

locus of non-proportional loading was remarkably different from proportional loading using micro-mechanical finite element analysis.

Note that for crushing behaviour, non-proportional loading is even more remarkable as a material point may vary from compression to shear, and even to tension [19]. For example, Hong et al. [55] investigated the crushing behaviour of aluminium honeycombs experimentally, indicating that non-proportionally combined loads had a significant influence on the folding patterns. However, in the context of phase field methods, non-proportional loading remains under-studied and the stress states presented in open literature did not involve significant variations [48,49].

This study aims to fill this knowledge gap by developing an explicit phase field fracture model specifically tailored for ductile fracture in a crushing scenario involving significant non-proportional loading. The remainder of this paper is structured as follows. Section 2 proposes an explicit phase field formulation for additively manufactured metallic materials. Section 3 introduces material specimen preparation, testing and material parameter calibration. Section 4 presents the experimental and numerical results of crushing behaviour under three-point bending and axial compression. The fracture mechanism will also be discussed in detail. Finally, Section 5 summarises the key findings of this work.

2. Explicit phase field fracture model for additively manufactured metals

An explicit phase field method is first formulated by deriving the governing equations for the displacement and phase fields. Then, the constitutive relations for additively manufactured metallic materials are incorporated into the explicit phase field framework. Finally, non-proportional loading history is highlighted for crushing simulations.

2.1. Energy functional

Let $\Omega \in \mathbb{R}^{dim}$ here (*dim* stands for the spatial dimension) be an arbitrary elastoplastic body with external boundary $\partial\Omega$ and internal discontinuity boundary Γ, as shown in Fig. 1. $\partial\Omega$ can be decomposed into Dirichlet boundary $\partial\Omega^h$ and Neumann boundary $\partial\Omega^s$ with the following relationship: $\partial\Omega^h \cap \partial\Omega^s = \varnothing$ and $\partial\Omega = \overline{\partial\Omega^h \cup \partial\Omega^s}$. The state of the system is described by the set of variables $X = \{\mathbf{u}, d, \bar{\varepsilon}^p\}$, where $\mathbf{u}$ denotes the displacement field, d represents the phase field, and $\bar{\varepsilon}^p$ is an internal state variable. d ranges from 0 to 1 with $d = 0$ denoting the intact state and $d = 1$ representing the fully broken state.

The elastic energy E_{elas} and plastic energy E_{plas} can be derived as:

$$E_{elas}(\mathbf{u}, \bar{\varepsilon}^p, d) = \int_0^t \int_\Omega (1-d)^2 \mathbf{D}^e : \widetilde{\sigma} \, d\Omega ds, \tag{1a}$$

$$E_{plas}(\mathbf{u}, \bar{\varepsilon}^p, d) = \int_0^t \int_\Omega (1-d)^2 \mathbf{D}^p : \widetilde{\sigma} \, d\Omega ds, \tag{1b}$$

where s is loading time with $0 \leq s \leq t$; and $\widetilde{\sigma}$ is undamaged stress with "$\widetilde{\blacksquare}$" denoting the quantities in an undamaged configuration. The damaged stress σ can be calculated as $(1-d)^2 \widetilde{\sigma}$ [56,57]. The rate of deformation $\mathbf{D}$ is given by $\partial\mathbf{v}/\partial\mathbf{x}$ with $\mathbf{v}$ and $\mathbf{x}$ being velocity field and spatial coordinates, respectively [58]. $\mathbf{D}$ may be additively decomposed into elastic part $\mathbf{D}^e$ and plastic part $\mathbf{D}^p$ as $\mathbf{D} = \mathbf{D}^e + \mathbf{D}^p$ under the hypoelastic-plasticity assumption [59].

The kinetic energy E_{kin} is given as:

$$E_{kin}(\dot{\mathbf{u}}) = \int_\Omega \frac{\rho \dot{\mathbf{u}} \cdot \dot{\mathbf{u}}}{2} \, d\Omega, \tag{2}$$

where $\dot{\mathbf{u}}$ is velocity and ρ is the mass density. The fracture energy is approximated as [3,57]:
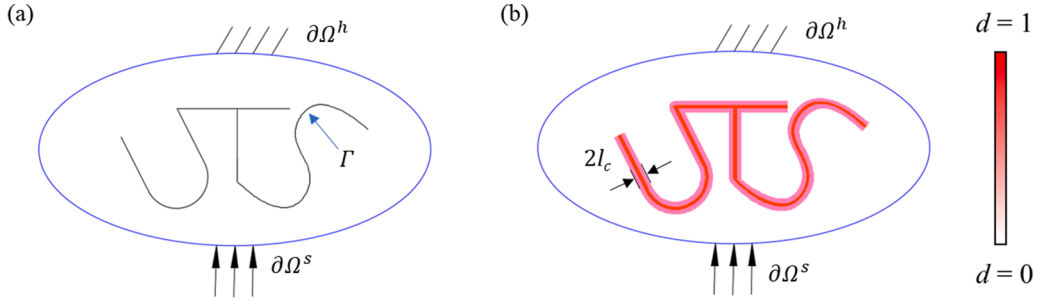
Fig. 1. Schematic illustration for the phase field model. (a) Sharp crack Γ is regularised by diffused crack (b) by introducing a phase field variable d. The crack width can be characterised by a length scale parameter l_c.

$$E_{frac}(d) \cong \int_{\Omega} \frac{g_f}{2l_c} \left(l_c^2 \nabla d \cdot \nabla d + d^2 \right) \, d\Omega, \tag{3}$$

where g_f is the critical energy release rate, l_c denotes the length scale parameter to control the diffusive crack width. Together with the degradation function $(1-d)^2$ in Eq. (1), the AT2 model is used in this study [1]. The viscous energy $E_{vis}(\dot{d})$ can be written as:

$$E_{vis}(\dot{d}) = \int_0^t \int_{\Omega} \frac{\omega}{2} \dot{d} \cdot \dot{d} \, d\Omega ds, \tag{4}$$

where ω denotes the artificial viscous parameter and is introduced to be compatible with the explicit finite element framework [36]. The external work can be derived as:

$$W_{ext}(\mathbf{u}) = \int_{\Omega} (\mathbf{f} \cdot \mathbf{u}) d\Omega + \int_{\partial\Omega^s} (\mathbf{t} \cdot \mathbf{u}) d\partial\Omega^s, \tag{5}$$

in which $\mathbf{f}$ and $\mathbf{t}$ are body force and boundary traction, respectively.

Finally, the total energy functional can be expressed as,

$$\Pi(\mathbf{u}, \, d, \, \overline{\varepsilon}^p) = E_{elas} + E_{plas} + E_{kin} + E_{frac} + E_{vis} - W_{ext}. \tag{6}$$

2.2. Governing equation

Following the standard finite element formulation [58], the governing equations for the displacement field in strong form are derived as:

$$\text{div}\boldsymbol{\sigma} + \mathbf{f} = \rho\ddot{\mathbf{u}} \text{ in } \Omega \times [0, t], \tag{7a}$$

$$\mathbf{n} \cdot \boldsymbol{\sigma} = \mathbf{t} \text{ on } \partial\Omega^s \times [0, t], \tag{7b}$$

$$\mathbf{u} = \underline{\mathbf{u}} \text{ on } \partial\Omega^h \times [0, t], \tag{7c}$$

where $\ddot{\mathbf{u}}$ is acceleration field, $\mathbf{n}$ denotes the outward normal to the boundary $\partial\Omega^s$, $\underline{\mathbf{u}}$ represents the displacement field on the boundary $\partial\Omega^h$. The governing equation for the phase field in strong form is given as:

$$\varpi\dot{d} = \begin{cases} 2(1-d)\mathscr{H}(\mathbf{u}, \overline{\varepsilon}^p) - (d - l_c^2 \nabla d \cdot \nabla d), & d < 1, \\ 0, & \text{otherwise,} \end{cases} \text{ in } \Omega \times [0, t], \tag{8}$$

where $\varpi = \omega l_c / g_f$ is a modified viscous parameter to be consistent with our previous work [48,50], and $\mathscr{H}(\mathbf{u}, \overline{\varepsilon}^p)$ is the crack driving force, which can be derived as:

$$\mathscr{H}(\mathbf{u}, \overline{\varepsilon}^p) := \max_{0 \le s \le t} (\mathscr{S}(\text{state}(\mathbf{u}, \overline{\varepsilon}^p))), \tag{9}$$

which is the maximum value of a state function $\mathscr{S}(\text{state}(\mathbf{u}, \overline{\varepsilon}^p))$ obtained in the full loading process $s \in [0, t]$:

$$S(\text{state}(\mathbf{u}, \overline{\varepsilon}^p)) = l_c \left/ g_f \int_0^s (\mathbf{D}^e + \mathbf{D}^p) : \widetilde{\boldsymbol{\sigma}} ds. \right. \tag{10}$$

2.3. Constitutive relations for additively manufactured metals

Metallic materials additively manufactured by LPBF was considered in this study and their plastic deformation of metals was assumed to be transversely isotropic due to the scanning strategy [50]. Suppose that the xy plane is the printing plane and z-axis refers to the building direction; and the transversely isotropic Hill48 yield function [60,61] can be expressed as:

$$\widetilde{f}(\widetilde{\sigma}) = \sqrt{\begin{array}{c} F\left[\left(\widetilde{\sigma}_{yy} - \widetilde{\sigma}_{zz}\right)^2 + \left(\widetilde{\sigma}_{zz} - \widetilde{\sigma}_{xx}\right)^2 \right] + H\left(\widetilde{\sigma}_{xx} - \widetilde{\sigma}_{yy}\right)^2 \\ + 2L\left[\widetilde{\sigma}_{yz}^2 + \widetilde{\sigma}_{zx}^2 \right] + 2N\widetilde{\sigma}_{xy}^2 \end{array}}. \tag{11}$$

The given equation involves the stress tensor $\widetilde{\sigma}$ and anisotropic parameters, namely F, H, L, and N. The normal stresses along the x, y, and z axis are represented by $\widetilde{\sigma}_{xx}$, $\widetilde{\sigma}_{yy}$, and $\widetilde{\sigma}_{zz}$, respectively, and the shear stress components are $\widetilde{\sigma}_{xy}$, $\widetilde{\sigma}_{yz}$, and $\widetilde{\sigma}_{zx}$.

As for fracture initiation, it is widely acknowledged that the fracture strain is strongly associated with stress states [23,51], which could be described by stress triaxiality η and Lode angle parameter $\overline{\theta}$. Typical stress states $(\eta, \overline{\theta})$, such as uniaxial tension (1/3, 1) and compression ($-1/3, -1$), shear (0, 0), equibiaxial tension (2/3, -1) and compression ($-2/3, 1$), are illustratively highlighted in Fig. 2. According to the value of stress triaxiality, high stress triaxiality ($\eta > 2/3$), medium stress triaxiality ($1/3 < \eta < 2/3$) tension, and tension-shear ($0 < \eta < 1/3$) are also frequently used in the literature [62–64]. Similarly, in the
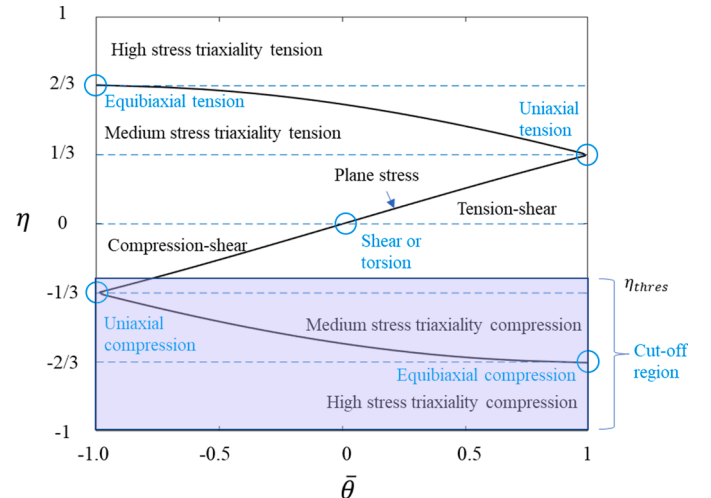

Fig. 2. Stress triaxiality and Lode angle parameter for typical stress states.

compressive region, high stress triaxiality ($\eta < -2/3$), medium stress triaxiality ($-2/3 < \eta < -1/3$) compression, and compression-shear ($-1/3 < \eta < 0$) can also be divided by η. Note that nevertheless, fracture is rarely initiated in experimental observations when $\eta < \eta_{thres}$, particularly for metallic materials. Hence, a cut-off value η_{thres} is commonly employed to regulate non-physical compressive damage [32,33]. Moreover, in the case of plane stress problems, the Lode angle parameter and triaxiality become dependent, and permissible stress states can be represented by the black line in Fig. 2 [51].

This present study utilised the Modified Mohr-Coulomb (MMC) model to capture the onset of cracking for LPBF 316L steel due to its proven accuracy, as noted in our previous work [50]. The fracture strain $\bar{\varepsilon}^f$ is defined as follows [65]:

$$\bar{\varepsilon}^f(\eta,\bar{\theta}) = \left\{ \frac{A}{c_2}\left[c_3 + \frac{\sqrt{3}}{2-\sqrt{3}}(1-c_3)\left(\sec\left(\frac{\bar{\theta}\pi}{6}\right)-1\right)\right]\left[\sqrt{\frac{1+c_1^2}{3}}\cos\left(\frac{\bar{\theta}\pi}{6}\right)+c_1\left(\eta+\frac{1}{3}\sin\left(\frac{\bar{\theta}\pi}{6}\right)\right)\right] \right\}^{-\frac{1}{n}}. \tag{12}$$

The equation requires calibration of two plastic parameters A and n, and three fracture parameters c_1, c_2, c_3.

As for the fracture initiation of Ti-6Al-4V titanium alloys, it is found that the Bao-Wierzbicki model [24] showed more acceptable accuracy, which revealed a three-branch empirical fracture locus of fracture strain with respect to stress triaxiality. In the high stress triaxiality region, an exponential function was used to describe the relationship between fracture strain and stress triaxiality due to void growth dominant fracture mechanism [66]. In the low stress triaxiality region, shear fracture was dominated, which can be described by a quadratic equation. In this case, the Bao-Wierzbicki model can be given as:

$$\bar{\varepsilon}^f(\eta) = \begin{cases} +\infty, & \eta < \eta_{thres}, \\ B_1\eta^2 + B_2\eta + B_3, & \eta_{thres} \le \eta \le 0.24, \\ B_4 + B_5 e^{B_6\eta}, & \eta > 0.24, \end{cases} \tag{13}$$

in which B_1, B_2, B_3, B_4, B_5, and B_6 are the material parameters and η_{thres} is the cut-off value for stress triaxiality.

2.4. Non-proportional loading history

To prevent non-physical damage evolution under small deformation, Eq. (10) is re-formulated as [48]:

$$S(\text{state}(\mathbf{u},\bar{\varepsilon}^p)) = (l_c / g_f)\tilde{\varphi}_{cr}\left\langle \int_0^s (\mathbf{D}^e+\mathbf{D}^p):\tilde{\boldsymbol{\sigma}}\mathrm{d}s \middle/ \tilde{\varphi}_{cr} - 1 \right\rangle, \tag{14}$$

in which $\tilde{\varphi}_{cr}$ is energy-based damage threshold, depending on the stress state [48,49], i.e., stress triaxiality η and Lode angle parameter $\bar{\theta}$ referring to Appendix A1 in [48] for their definition.

In practical applications, especially for crushing simulations [19,55], non-proportional loading conditions are quite common [25,67]. It means that the stress state of a material point varies, for example from compression to shear and tension, during such a loading history, leading to evolving fracture strains. Therefore, it is essential to incorporate a loading history-dependent damage indicator D [49,65]:

$$D(\bar{\varepsilon}^p) = \int_0^{\bar{\varepsilon}^p} \frac{\mathrm{d}\bar{\varepsilon}^p}{\bar{\varepsilon}^f(\eta,\bar{\theta})}. \tag{15}$$

Once $D = 1$, phase field d starts evolving. Damage indicator D is used to determine the fracture initiation, while phase field d represents the state of damage. Although both varies from 0 to 1, they have different physical meanings. A conceptual diagram illustrating the proposed model can be referred to in Fig. 3a [50]. There are three stages in the whole loading process, i.e., elastic stage $\mathbb{E}$, elastoplastic stage $\mathbb{EP}$ and elastoplastic-damage stage $\mathbb{EPD}$. When the stress goes beyond the initial yield stress, the plasticity occurs and the damage indicator D begins to accumulate until reaching 1 when damage initiates. Subsequently, phase field d starts to evolve from 0 to 1, as evident in Fig. 3b.

Fig. 4 illustrates the concepts of proportional and non-proportional loadings in damage threshold-based phase field models. In the previous phase field framework [12,68,69], the damage threshold was treated as a constant, visually depicted by the pink horizontal line in
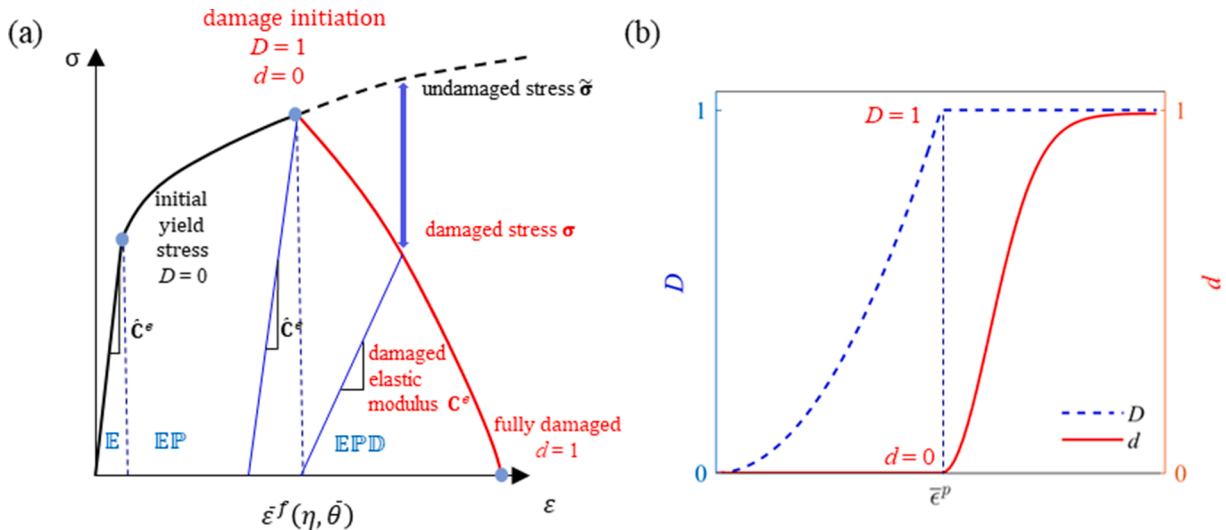

Fig. 3. Conceptual illustration of the proposed phase field model for ductile fracture. (a) stress-strain response; (b) Evolution of damage indicator and phase field.
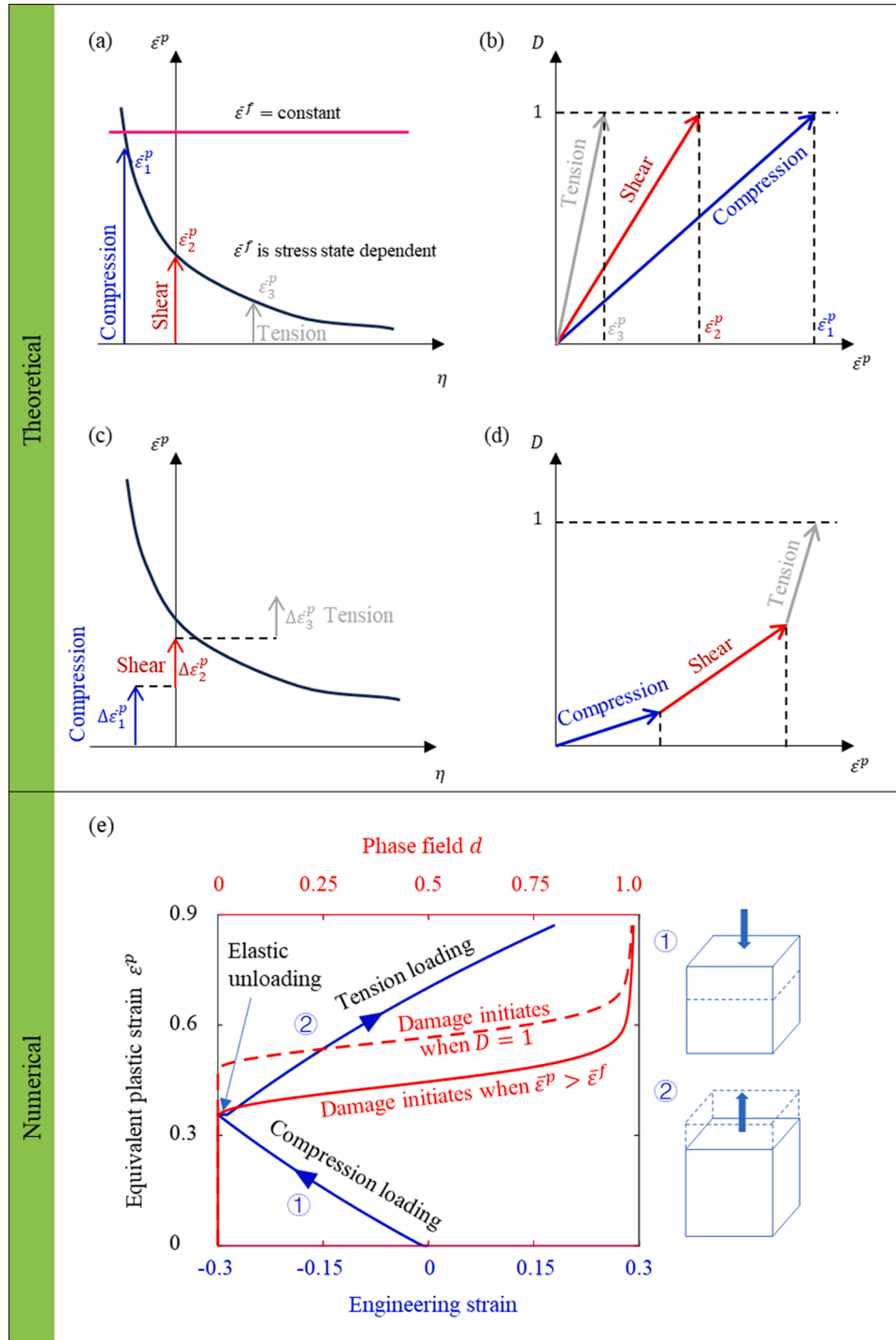
Fig. 4. Schematic of proportional and non-proportional loadings and fracture initiations. (a) fracture locus and proportional loadings of compression ($\bar{\varepsilon}_1^p$), shear ($\bar{\varepsilon}_2^p$), and tension ($\bar{\varepsilon}_3^p$), respectively; (b) damage indicator D versus equivalent plastic strain $\bar{\varepsilon}^p$ under proportional loading; (c) fracture locus and non-proportional loading varying from compression ($\Delta\bar{\varepsilon}_1^p$) to shear ($\Delta\bar{\varepsilon}_2^p$) and then tension ($\Delta\bar{\varepsilon}_3^p$); (d) damage indicator D versus equivalent plastic strain $\bar{\varepsilon}^p$ under non-proportional loading; (e) Numerical example of one element. Blue line illustrates the loading process of compression, unloading, and tension in sequence; phase field evolution without and with considering non-proportional loading history are represented via red solid and dashed line, respectively.

Fig. 4a. As discussed in [48,49], the threshold should depend on the stress state, illustrated by the black curve in Fig. 4a and c. Under proportional loading, such as pure compression ($\bar{\varepsilon}_1^p$), shear ($\bar{\varepsilon}_2^p$), and tension ($\bar{\varepsilon}_3^p$) with a constant stress triaxiality throughout the loading process (refer to Fig. 4a), the damage indicators increase linearly until reaching 1, but with different slopes due to different fracture strains, as displayed in Fig. 4b. It can be seen from Fig. 4a that the fracture initiations exactly

locate on the fracture locus as $D = 1$ is equivalent to $\bar{\varepsilon}^p = \bar{\varepsilon}^f(\eta, \bar{\theta})$ for proportional loadings.

For non-proportional loading, e.g., starting with compression ($\Delta\bar{\varepsilon}_1^p$) and transitioning to shear ($\Delta\bar{\varepsilon}_2^p$) and then tension ($\Delta\bar{\varepsilon}_3^p$) (see Fig. 4c), the accumulation of the damage indicator can also be divided into three stages, as illustrated in Fig. 4d. The accumulations exhibit varying slopes due to different fracture strains under distinct loading conditions.

Furthermore, as observed in Fig. 4c, the fracture initiation does not locate on the fracture locus as it becomes loading history dependent.

Once damage initiates, the energy-based damage threshold $\widetilde{\varphi}_{cr}$ can be written as:

$$\widetilde{\varphi}_{cr} = \int [(\mathbf{D}^e + \mathbf{D}^p) : \widetilde{\sigma}] dt \mid_{D=1}. \tag{16}$$

With the above theoretical formulation at hand, a staggered algorithm was used in numerical implementation here for its proven robustness [70]. User-defined subroutines VUMAT and VUEL with ABAQUS/Explicit solver were utilised to calculate displacement and phase fields, respectively [40]. To transfer the data between VUMAT and VUEL, a global module as well as user subroutines VUSDFLD and VUFIELD were adopted [40].

To further explain the necessity of considering non-proportional loading, a special case of numerical example is provided Fig. 4a. Consider an element subjected to a sequence of compressive loading (engineering strain of -0.3), elastic unloading and reverse loading (uniaxial tension) up to a strain of 0.2. The fracture strains are $\bar{\varepsilon}_1^f = 0.6$ under uniaxial compression and $\bar{\varepsilon}_3^f = 0.3$ under uniaxial tension. If the history of non-proportional loading is not considered, fracture initiates under the condition of $\bar{\varepsilon}^p \geq \bar{\varepsilon}^f(\eta, \bar{\theta})$ that is checked at every instant. At the compressive loading, fracture cannot initiate as the maximum equivalent plastic strain 0.36 is smaller than the compressive fracture strain 0.6. Once it is reverse loaded after elastic unloading, fracture initiation immediately occurs as the equivalent plastic strain accumulated in compressive loading is larger than the tensile fracture strain 0.2. This abrupt change to fracture initiation is non-physical as the tension loading has not led to any plastic or even elastic deformation yet. In contrast, when the history of non-proportional loading is considered, the damage indicator accumulates until $D = \Delta\bar{\varepsilon}_1^p / \bar{\varepsilon}_1^f + \Delta\bar{\varepsilon}_3^p / \bar{\varepsilon}_3^f = 1$. Subsequently, the evolution of phase field occurs later than the case without considering non-proportional loading history.

3. Material testing and model calibration

Material specimens of additively manufactured 316L steel and Ti-6Al-4V titanium were fabricated and tested. The explicit phase field model was calibrated for both materials using experimental tests in this section.

3.1. Sample preparation from additive manufacturing

To investigate the crushing behaviour of 3D printed metallic materials, two commonly utilised materials, namely 316L steel and Ti-6Al-4V titanium, were fabricated by LPBF using the commercial printer EOS M290 (EOS GmbH, Krailing, Germany). The chemical compositions of the two powders are listed in Table 1. Argon atmosphere was employed to safeguard the materials against oxidation. The scanning electron microscopy (SEM) images of the two powders are displayed in Fig. 5. The particles exhibit smooth, ball-shaped surfaces, indicating excellent mobility and meeting manufacturing requirements.

The printing parameters for both materials were identical, with a laser power of 280 W and a scanning speed of 1200 mm/s. The hatching space and layer thickness were set at 0.14 mm and 30 μm, respectively. Post-heat treatments for both materials were conducted in a furnace. In the case of the printed 316L samples, the temperature was gradually increased from approximately 10 °C (room temperature) to 400 °C over

a span of 60 min, with a heating rate of 6.5 °C/min. The specimens were then maintained at 400 °C for 4 h before being cooled to room temperature at an average rate of 1 °C/min. For LPBF Ti-6Al-4V, the temperature was raised from room temperature (around 10 °C) to 800 °C within 90 min with a heating rate of 8.8 °C/min. The specimens were subsequently held at 800 °C for 2 h in the furnace before being cooled to room temperature at an average cooling rate of 9.875 °C/min.

3.2. Material specimens and calibration

The material characterisation was conducted using five different groups of specimens [50], each with a unique stress state, i.e. uniaxial tension (UT), simple shear (SS), notched tension with a 5 mm radius (NTR5), notched tension with a 20 mm radius (NTR20), and tension specimen with a central hole (CH), as depicted in Fig. 6a–e. These specimens cover a wide range of stress states and have a uniform thickness of 1.68 mm for 316L and 1.77 mm for Ti-6Al-4V. All specimens were printed with their axial direction oriented at 90° with respect to the building direction. Additionally, UT specimens were printed along directions of 0° and 45° with respect to the building direction.

Elastoplastic parameters were determined from UT specimens. In specific, 90° UT specimens were used to determine the elastic properties, i.e., Young's modulus $\widetilde{E}$ and Poisson's ratio ν. Additionally, 0° and 45° UT specimens were employed to calibrate anisotropic parameters F, H, L, and N of the transversely isotropic Hill48 yielding model [50]. The strain hardening curves for 316L steel and Ti-6Al-4V titanium are presented in Fig. A1.

Fracture initiation parameters were calibrated via all five groups of samples. The MMC parameters of 316L steel can be referred to in our previous work [50]. For Ti-6Al-4V titanium, the same calibration procedure was used to determine the Bao-Wierzbicki model. The fracture initiation parameters were determined via the least-square method such that the damage indicator D in the simulations was as close to 1 as possible at the instant of fracture initiation in the experiments for all N sets of tests (here $N = 5$) as follows:

$$[B_1, B_2, B_3, B_4, B_5, B_6] = \underset{B_1, B_2, B_3, B_4, B_5, B_6}{\mathrm{argmin}} \left(\frac{1}{N} \sum_{i=1}^{N} (D-1)^2 \right) \tag{17}$$

The length scale parameter l_c was selected to be 0.5 mm for both materials to reproduce the experimental data [50]. Regarding the critical energy release rate g_f, it was determined by matching the descending branch of force-displacement curves, referring to their bounds from [71, 72]. Note that in their studies, g_f varied with loading, meaning that the value of g_f changed during crack propagation. Dittmann et al. [73] proposed a degradation function for g_f with respect to plastic work density. Similarly, Yin and Kaliske [74] degraded g_f by hardening as a function of the von Mises equivalent plastic strain. In our study here, however, g_f was treated as a constant for simplicity, which was able to fairly reproduce experimental crack propagation for both materials. Yet, it would be an interesting topic to explore the influence of a varying g_f on phase field models in the future.

The calibrated material parameters are given in Table 2.

3.3. Simulation results

In this study, the 8-node linear brick elements with reduced integration (C3D8R) were used for all finite element models and an element size of 0.15 mm were adopted in the localised region in Abaqus/Explicit.

Table 1
Chemical compositions of 316L and Ti-6Al-4V powder (wt%).

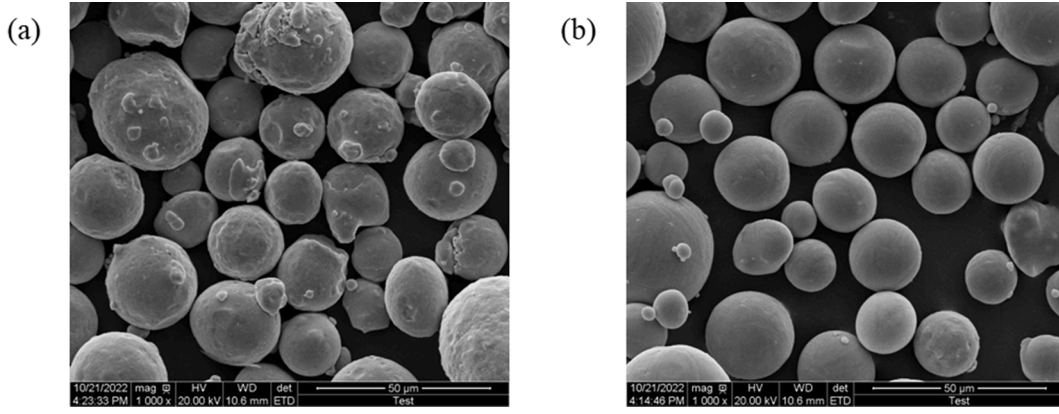| 316L	Element	Cr	Ni	Mo	Mn	Si	C	P	S	O
	Content	16-18	10-14	2-3	<2	<1	<0.03	<0.045	<0.03	<0.1
Ti-6Al-4V	Element	Al	V	C	Fe	O	N	H		
	Content	5.5-6.75	3.5-4.5	<0.08	<0.3	<0.15	<0.05	<0.015		

Fig. 5. SEM micrographs. (a) 50 μm scale 316L powder; (b) 50 μm scale Ti-6Al-4V powder.
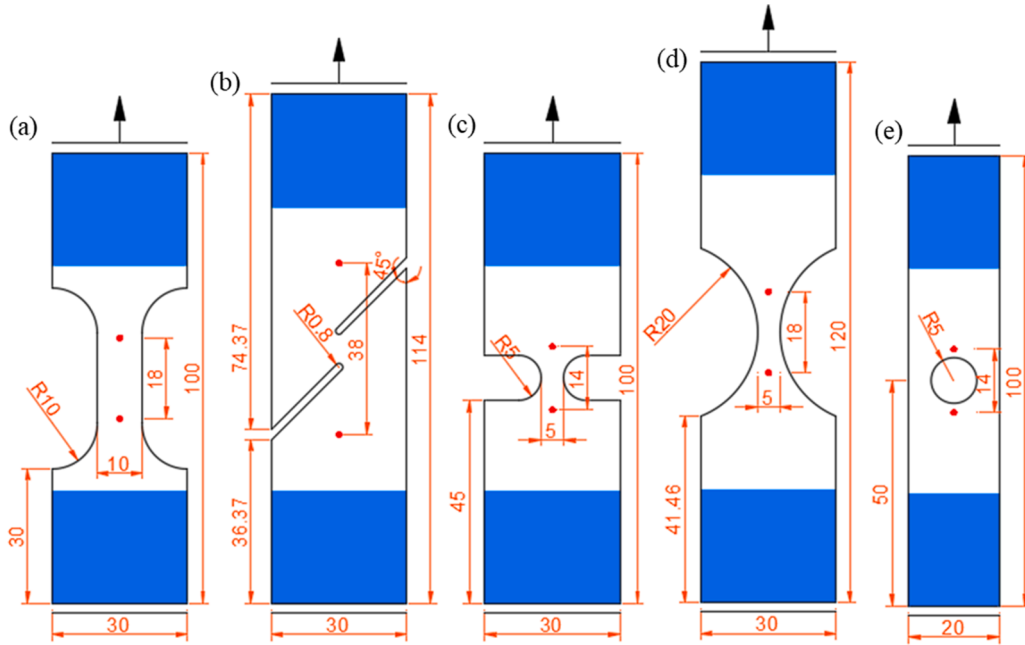

Fig. 6. Specimens designed for material calibration for both 316L steel and Ti-6Al-4V titanium (unit: mm) [50]: (a) uniaxial tension, (b) simple shear, (c) notched tension with a 5 mm radius, (d) notched tension with a 20 mm radius, and (e) tension specimen with a central hole. The red dots indicate the measurement points of displacement. The UT specimens were printed in 0°, 45°, and 90° orientations to calibrate the transverse Hill48 plastic model. The UT specimen, together with the other specimens printed in 90° orientation, was utilised to calibrate the fracture initiation model.

All the material specimens were full fixed at the bottom and loaded at the top with a speed of 0.2 m/s. Note the when the explicit phase field model is used for the quasi-static analysis, the loading velocity may be larger than the experimental counterpart to improve computational efficiency. The kinetic energy E_{kin} (see Eq. (2)) was found sufficiently small to minimise the dynamic effect [41].

3.3.1. Calibrated force-displacement curves

The force-displacement responses of 316L steel specimens are plotted in Fig. 7. For all the 316L steel specimens, the global force increased linearly until the plastic yielding point. Apparently, the numerical and experimental data exhibited a high degree of agreement, indicating the accuracy of the elastic parameters. Subsequently, the plastic stage was reasonably predicted by the transversely isotropic Hill48 model and extrapolated hardening curve, especially for UT, SS, and NTR20. As for fracture initiation, it can be found that the modified Mohr-Coulomb model exhibited good predictability from the solid circles and pentagrams, as shown in Fig. 7. The average error for all five specimens was around 3.24%. Nevertheless, predicting errors can still be

observed. For example, the simulated fracture initiation of SS sample was slightly earlier than its experimental counterpart, which may be because the fracture strain under shear stress state in the model was compromised to take a small value in order to consider other stress states. On the contrary, for NTR20 specimen, the fracture strain in the simulation seemed to be calibrated with a large value. The descending branches were also well captured by the proposed phase field model using the calibrated parameters, suggesting the accuracy of the proposed model.

As pointed out by Miehe et al. [70], the artificial viscous parameter ω could significantly influence the mechanical response. The viscous parameter ω was originally introduced by Miehe et al. [57,70] to facilitate numerical implementation. The viscous regularisation is convenient for implementation of explicit algorithms [36,40] and can stabilise numerical solutions [70]. When the viscous parameter approaches 0, the model tends to predict a steep load drop, while the a slightly larger viscous parameter is able to smooth out the brutal crack evolution [70].

To determine the value for ω, a parametric analysis was conducted using UT specimens of 316 steel. The viscous parameter ω was set to 4

Table 2

Material parameters for additively manufactured 316L steel [50] and Ti-6Al-4V titanium.

		316L Parameters	Value [50]	Ti-6Al-4V Parameters	Value
Elasticity	$\widetilde{E}$		145000.0 MPa	$\widetilde{E}$	110000.0 MPa
	ν		0.3	ν	0.3
Transversely isotropic Hill48 yielding function	F		0.50	F	0.50
	H		0.39	H	0.45
	L		1.45	L	1.03
	N		1.50	N	1.50
Damage initiation	A		1338.9 MPa	B_1	1.73
	n		0.7	B_2	-0.02473
	c_1		0.01	B_3	0.0928
	c_2		465.7 MPa	B_4	0.0373
	c_3		0.74	B_5	0.0000463
	η_{thres}		-0.33	B_6	-5.624
				η_{thres}	-0.33
Damage evolution	l_c		0.5 mm	l_c	0.5 mm
	g_f		15 N/mm	g_f	1 N/mm

$\times 10^{-5}$, 2×10^{-4}, 1×10^{-3}, and 5×10^{-3} kN·s/mm². The corresponding force-displacement curves are presented in Fig. 7a. Before fracture initiation, the force-displacement curves coincided as expected owing to the identical elastoplastic parameters. After fracture initiation, a smaller viscous parameter ω resulted in a more rapid decrease in global force. When $\omega = 2 \times 10^{-4}$ kN·s/mm², the difference was negligible compared with the case when $\omega = 4 \times 10^{-5}$ kN·s/mm².

Furthermore, Hu et al. [41] suggested that the determination of ω should satisfy that the ratio of the artificial viscous energy E_{vis} to external work W_{ext} is sufficiently small (e.g., <15%). In this study, the viscous parameter ω was determined based on parametric study and the ratio of E_{vis}/W_{ext}. The values for 316L steel and Ti-6Al-4V titanium were set to 2×10^{-4} and 3×10^{-5} kN·s/mm², respectively.

Since explicit methods are conditionally stable, the critical stable time increment needs to be determined by considering both the displacement and phase field sub-problems [36,41,75]. In this study, the critical stable time increment for the displacement field sub-problem $\Delta t_\mathbf{u}$ was always smaller than that for the phase field sub-problem Δt_d, meaning that the critical stable time increment was controlled by displacement field. The critical stable time increment was calculated as 4×10^{-8} s for 316L steel and 3.45×10^{-8} s for Ti-6Al-4V titanium, respectively. When the time increment was smaller than this critical value, the force-displacement curves were identical.

The force-displacement curves of Ti-6Al-4V titanium specimens are presented in Fig. 8. Similarly, the elastic stages were perfectly predicted by the numerical model. Due to the brittleness of Ti-6Al-4V titanium, necking behaviour was negligible. Therefore, the predicted plastic stage was somewhat more accurate than that for 316L. The hardening curve was provided in Fig. A1.

Further, the Bao-Wierzbicki model exhibited high accuracy for fracture initiation of Ti-6Al-4V titanium material samples with an average error of 5.16%. As for the damage evolution, unfortunately, the experimental data was missing due to the abrupt rupture. Unlike 316L steel, the critical energy release rate and viscous parameter cannot be determined from material specimens. Therefore, these two parameters will be determined via structural specimens in Section 4.

3.3.2. Crack paths

Fig. 9 compares the experimental and numerical cracks for both 316L steel and Ti-6Al-4V titanium. All the crack paths could be well predicted. For instance, SS specimens exhibited vertical crack paths due to shear loading, while NTR5, NTR20, and CH20 specimens presented horizontal crack paths caused by medium stress triaxiality tension. Interestingly, for the UT specimen, 316L steel exhibited a purely horizontal crack path

while Ti-6Al-4V contained an inclined crack path, agreeing with experimental observations. The inclined crack path in Ti-6Al-4V titanium was found to be caused by shear stress state. For 316L steel, the crack was induced by pure uniaxial tension. Moreover, 316L steel exhibited higher ductility than Ti-6Al-4V titanium, experiencing large plastic deformation, more pronounced necking and less localised cracks for all material samples.

4. Crushing simulation for 3D printed tubes

This section aims to investigate the crushing behaviour of LPBF additively manufactured 316L steel and Ti-6Al-4V titanium tubes. For the 316L steel tube, global responses, crack formation and underlying failure mechanisms for both three-point bending and axial compression will be discussed. For the Ti-6Al-4V titanium tube, the three-point bending will be analysed. Last, the fracture mechanism for both materials will be explored thoroughly.

4.1. Experimental and modelling setup

In this study, the three-point bending and axial compression of 316L steel tubes were studied. To compare different materials, three-point bending of Ti-6Al-4V titanium tubes was also performed with the same geometry and loading conditions as the 316L steel counterparts. The three-point bending and axial compression tests were conducted via an Instron 3369, as shown in Fig. 10, with a loading speed of 3 mm/min. Two cameras were positioned on the frontal and the left sides of the samples to capture the detailed deformation process; at the same time, the displacement and reaction force were recorded during compression tests.

To simulate the abovementioned tubal structures, the geometries, loading and boundary conditions were modelled as shown in Fig. 10. In the three-point bending and axial compression specimens, central square holes and rectangular grooves were respectively cut by a wire electrical discharge machine in order to trigger damage. Note that the loading direction was normal to the 3D printing direction in three-point bending tests, but parallel to the printing direction for the axial compression tests. The specimens were discretised with a mesh size of 0.2 mm in the crack propagation region. For enhancing computational efficiency, a one-quarter model for both tubal structures was used by taking advantage of symmetric geometry and loading conditions [19], which has been validated by our full-scale models. The material parameters are given in Table 2 and Fig. A1.

4.2. Crushing behaviour of 316L tube

4.2.1. Three-point bending

The numerical and experimental results regarding force-displacement curves of the top rigid indenter, energy ratios of kinetic energy and viscous energy to external work, and deformation contours of the 316L tube subject to three-point bending are shown in Fig. 11 and Fig. 12, respectively. From Fig. 11a, good agreement in terms of the force-displacement curves between the numerical results and experimental data can be observed. Fig. 11b indicates that kinetic and viscous energies were sufficiently small (less than 2% and 0.2%, respectively), guaranteeing quasi-static loading and acceptable artificial viscous energy.

As illustrated in Fig. 11a, the whole loading process can be divided into six stages as per the turning points of the simulated force-displacement curve. In the initial stage, numerical results showed a dominance of elastic deformation. The global force exhibited a nearly linear increase at the beginning. Subsequently, the global force continued rising, albeit with a reduced slope, until reaching the first peak (point i) seen in both the modelling and experimental results. This behaviour was attributed to local indentation and plastic deformation of the top wall under the indenter, as illustrated at instant i in Fig. 11a.
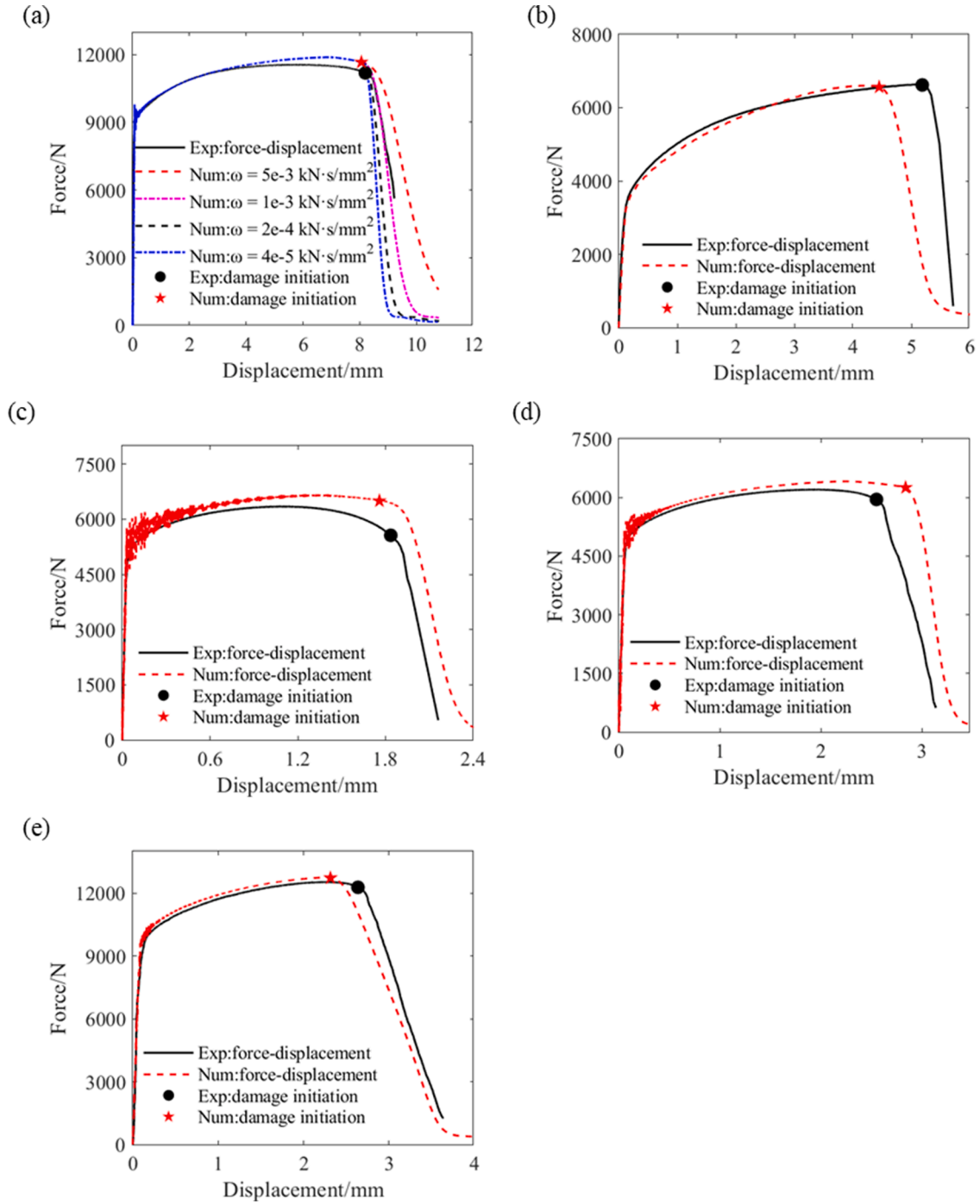
Fig. 7. Comparison of the experimental and numerical force-displacement responses of additively manufactured 316L material specimens. (a) UT specimen; (b) SS specimen; (c) NTR5 specimen; (d) NTR20 specimen; (e) CH specimen. Evidently, the experimental data could be properly reproduced by the proposed phase field model. Parametric study of viscous parameters for UT specimen was conducted in Fig. 7a. ω was set to 2×10^{-4} kN $\cdot$ s/mm^2 as per the difference could be negligible compared to simulated result with with the case when $\omega = 4 \times 10^{-5}$ kN $\cdot$ s/mm^2.

In Stage II, the global force exhibited a significant decline as a result of the further indentation on the top wall and the bending of the side walls. The predicted global response and deformation aligned well with the experimental data, as depicted in Fig. 11a, and seen at instant ii of Fig. 12.

In stage III, the load gradually decreased as a result of changing from local bending on the side walls to global bending of the tube, as seen at moment iii of Fig. 12. The numerical model accurately predicted both force-displacement curves and overall deformation. Despite the pronounced localisation of plastic deformation, the numerical results showed no signs of damage initiation, owing to the implementation of a stress triaxiality cut-off value.

In Stage IV, the global force is found to gradually increase. From the fourth row of Fig. 12a and b, the global bending further developed, which also triggered crack initiations around the top corners of the square holes, as seen in Fig. 12c. The cracks were caused by medium stress triaxiality tension based on the numerical simulation. Furthermore, it is worth noting that the crack initiated on the inner surface and propagated to the outer surface. The reason was that the inner surface was subject to tensile loading, where damage was generated easily. In
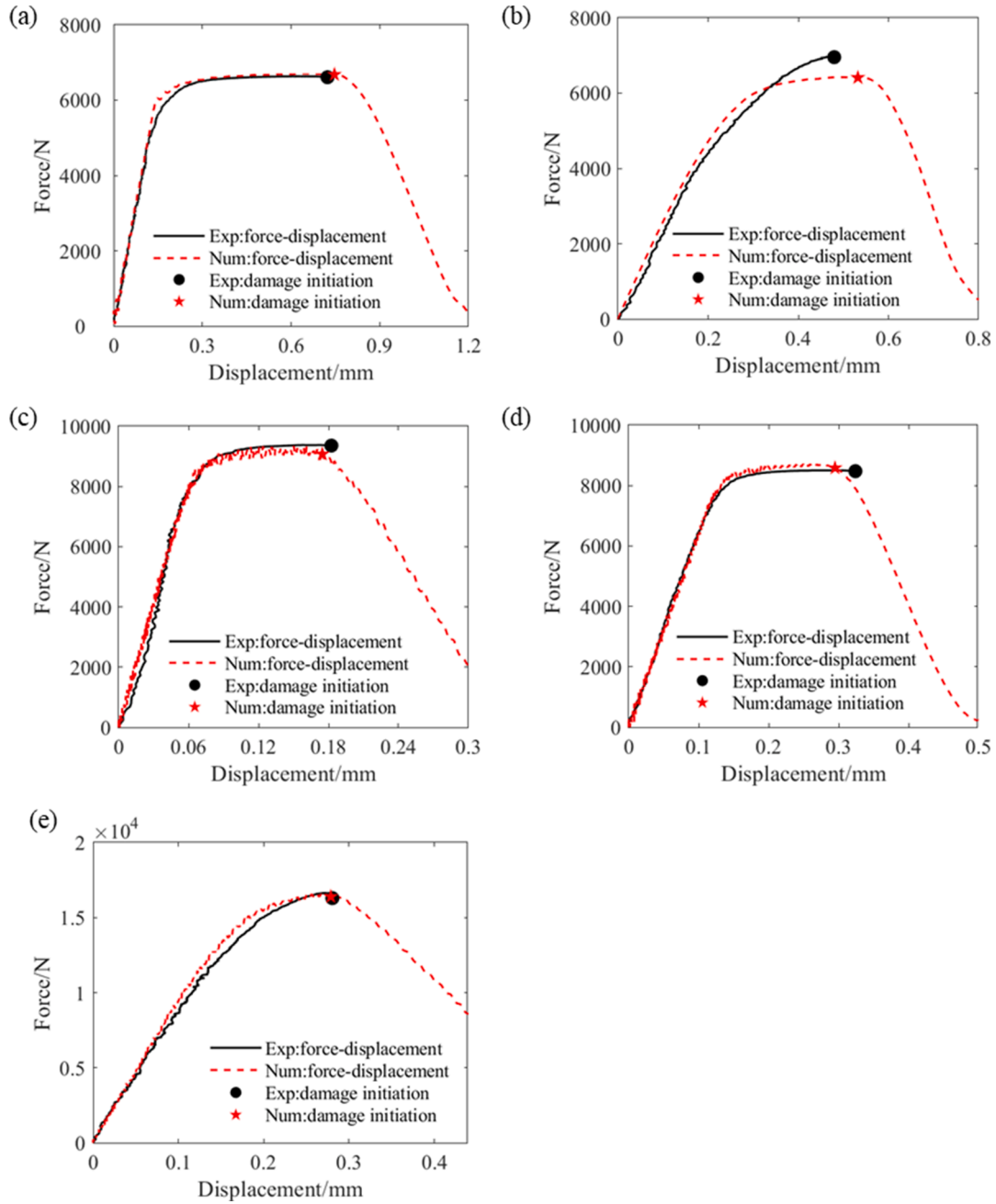
Fig. 8. Comparison of the experimental and numerical force-displacement responses of additively manufactured Ti-6Al-4V titanium material specimens. (a) UT specimen; (b) SS specimen; (c) NTR5 specimen; (d) NTR20 specimen; (e) CH specimen. Apparently, the experimental data could be properly reproduced by the proposed phase field model.

this stage, although the force-displacement curve deviates to a certain extent as seen in Fig. 11a, the numerical simulation effectively replicated the experimental observations concerning both the cracks and the overall deformation.

In Stage V, the global force further increased with a large slope due to the further development of the global bending (see Fig. 12v) until the second peak at point V, which was 12981.3 N when u=22.69 mm and 13662.6 N when u= 23.92 mm in the numerical simulation and experimental test, respectively. The prediction error was around 4.99% and 5.15% for the load and displacement, respectively, indicating the sufficiently high accuracy of the proposed model.

In the last stage, the global force started dropping again due to the deformed tube moving downward away from the supports.

Overall, the numerical modelling provided a fairly good prediction for the three-point bending of the 316L tube in terms of force-displacement response and deformation. It is noted that the plastic deformation was dominant throughout its loading process on account of its excellent ductility. Nevertheless, damage initiation and evolution could still be observed. To better demonstrate the proposed explicit phase field model, we also studied the three-point bending of Ti-6Al-4V tube in Section 4.3, which is much more brittle than 316L in general. The mechanism of damage will be further discussed in Section 4.4.

4.2.2. Axial compression

Fig. 13a presents the force-displacement curves recorded from the top loading platen. Overall, the numerical results agreed with the experimental data. According to Fig. 13b, it can be also seen that the kinetic and viscous energies were small enough (less than 5%) in
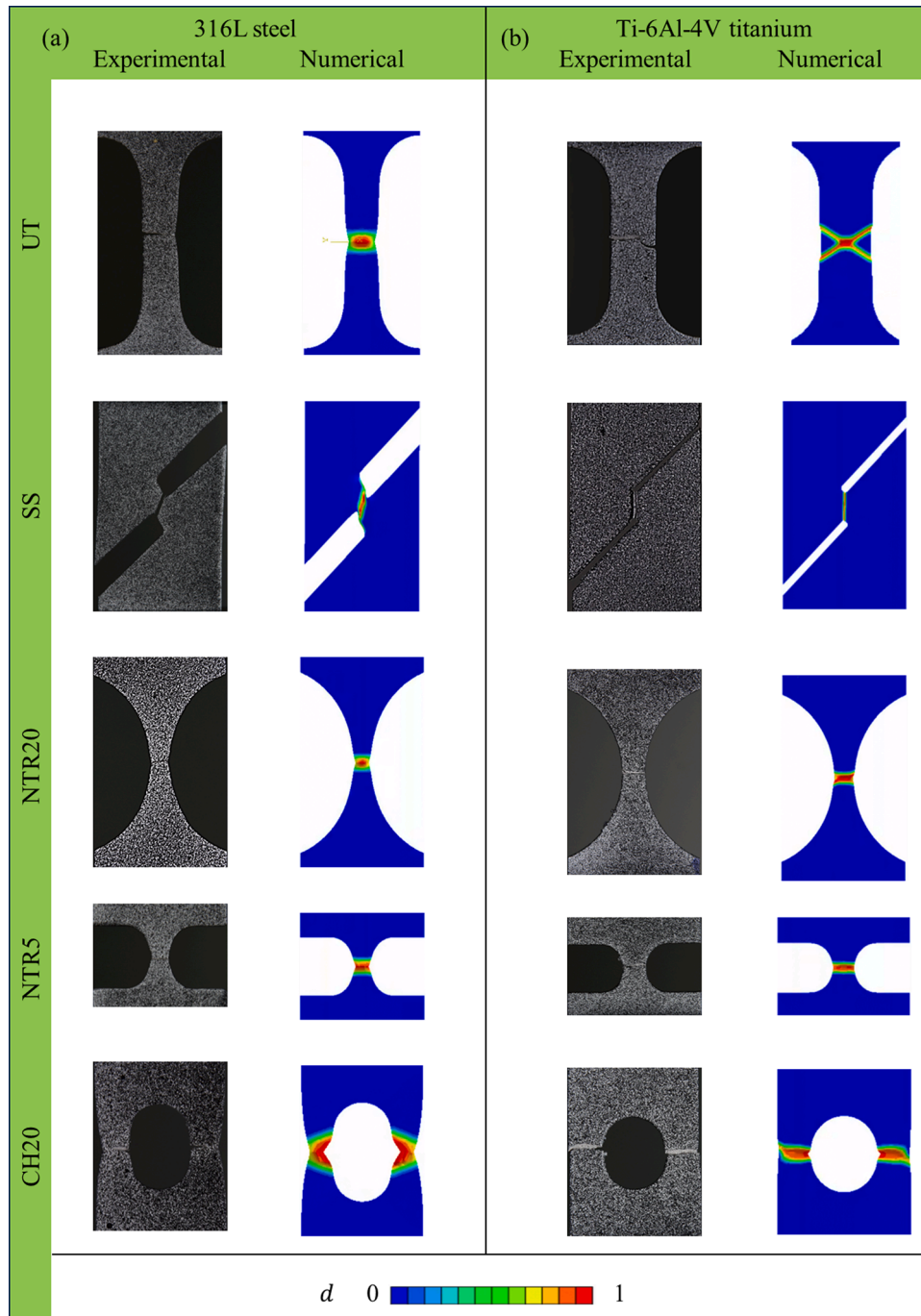
Fig. 9. Comparison of final cracks. The experimental and numerical cracks of (a) 316L steel and (b) Ti-6Al-4V titanium. Good agreements in terms of crack paths can be found. Compared with Ti-6Al-4V titanium, 316L steel had higher ductility, thus presenting more pronounced necking and less localised cracks.

comparison with the external work such that quasi-static loading condition can be guaranteed and artificial energies be negligible. The local peak and valley forces were related to the fold and crease formation of the tube. For the sake of a detailed analysis of crushing behaviour, Fig. 14 displays the deformation patterns at the local extremum of force from the numerical simulation, together with the equivalent plastic strain contours in the undeformed configuration, and phase field damage contours in both undeformed and deformed configurations.

Similarly, Fig. 13a can be divided into several distinctive crushing stages. Stage I was dominated by the elastic deformation, leading global force to increasing linearly until reaching the first peak load. Although the predicted displacement was slightly different from its experimental counterpart due to the fixture deformation of the testing machine, the predicted peak load showed fairly high accuracy with a 2.6% relative error, as shown in Fig. 13a.

In Stage II, the force started dropping due to local bending around the pre-existing rectangular groove. It also led to generation of the first fold, i.e., the left wall deformed outward at A, which was in good agreement with the experimental results (see instant ii in Fig. 14). Then, the force increased again partially because the upper and bottom surfaces of the groove contacted with each other, providing higher resistance in the loading direction. However, in the experimental results, there was no contact observed at this stage, which accounted for a lower load. Nevertheless, the force-displacement curves and deformations in the above stages were well predicted by the proposed phase field model, as shown in Fig. 13a.
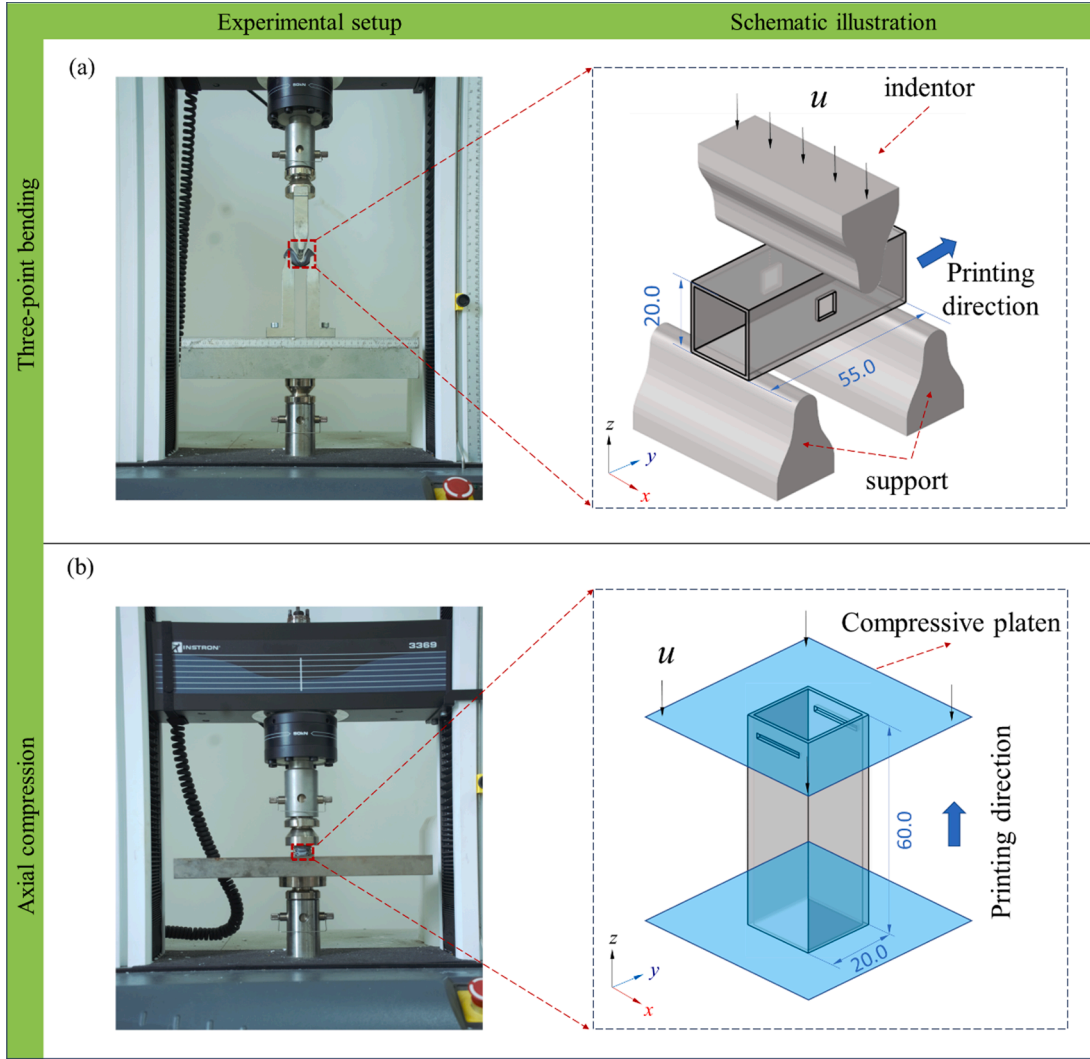
Fig. 10. Experimental and numerical setups for tubal structures. (a) three-point bending and its schematic of both 316L steel and Ti-6Al-4V titanium tubes. Central square holes were situated at the center of the plane with a side length of 6 mm. (b) axial compression and its schematic illustration of 316L tube. The pre-existing rectangular grooves had a dimension of 1.5×14 mm, and their upper edges were positioned 4 mm from the top surface of the tube. The wall thickness of the tubes was 1 mm.
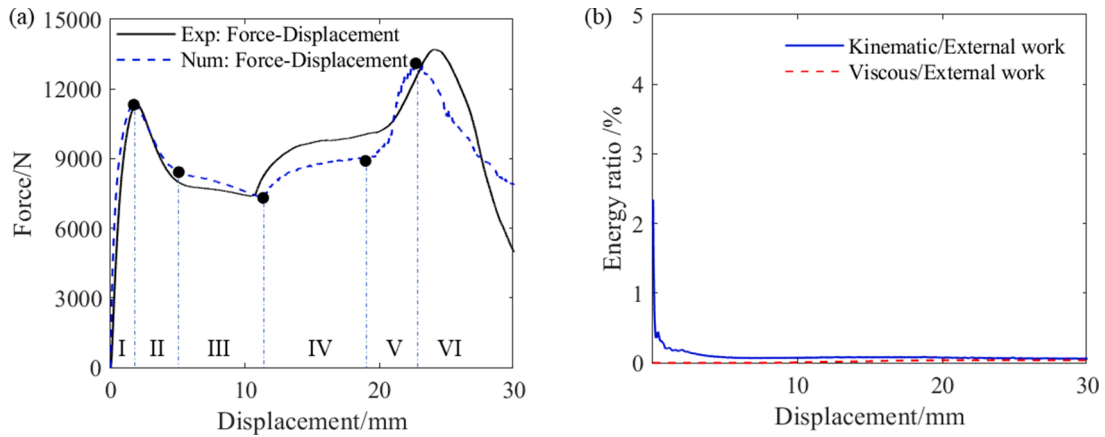

Fig. 11. Three-points bending loading of 316L tube. (a) force versus displacement curves; (b) ratios of kinetic and viscous energies to external work versus displacement curves. Force-displacement response of each stage was well predicted by the proposed phase field model. Kinetic and viscous energy were negligible compared to external work, indicating the simulation was reliable for quasi-static analysis.
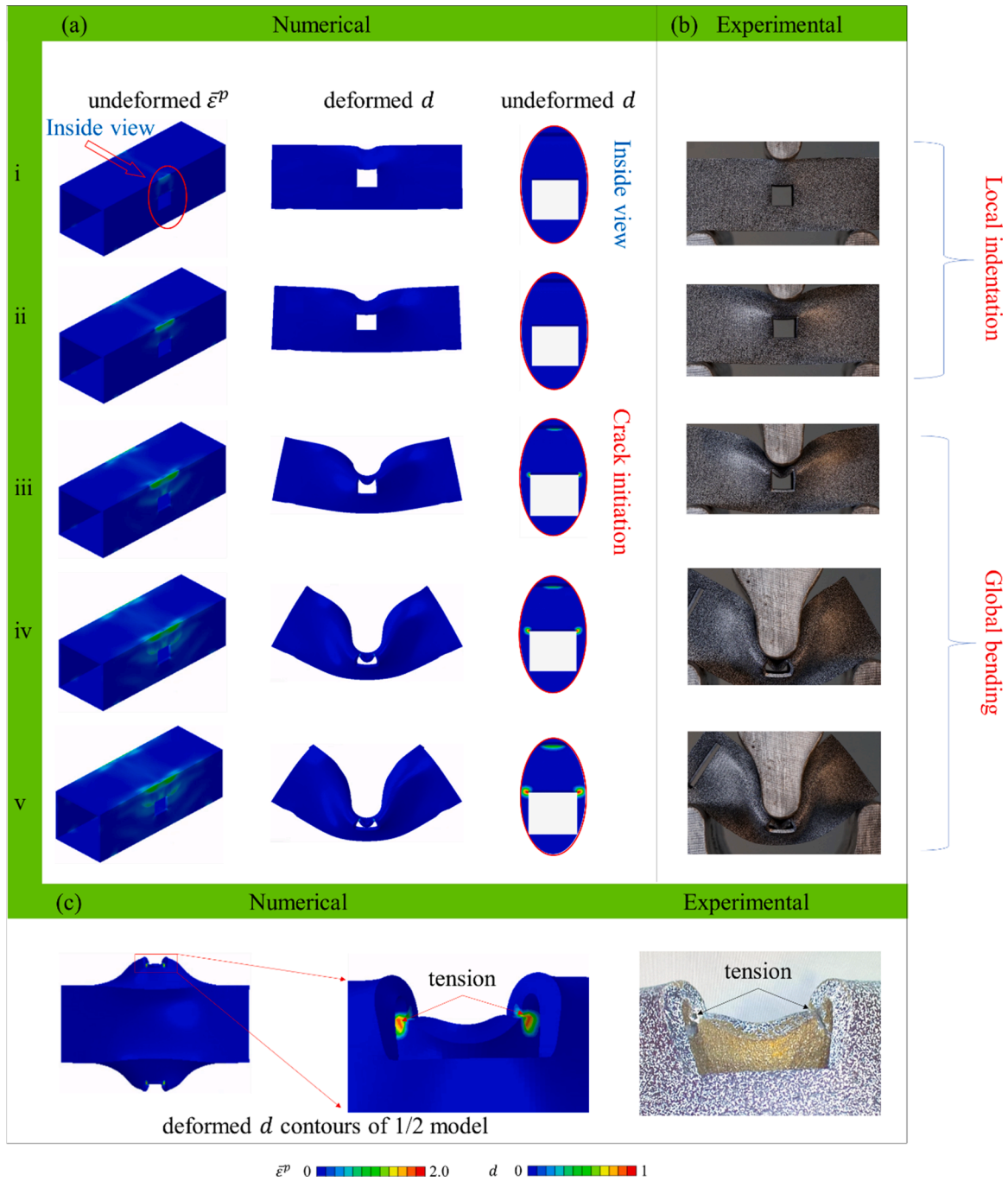
Fig. 12. Three-point bending analysis of 316L steel tube. (a) numerical contours of the equivalent plastic strain and phase field; (b) experimental results; (c) Final cracks in numerical and experimental results. The Roman lowercase numerals i-v denote the ends of the corresponding stages represented by the uppercase indices I-V in Fig. 11. Good agreement between numerical and experimental results in deformation mode and crack development could be observed.

In Stage III, the simulated global force decreased again, while the experimental counterpart decreased sharply in the beginning and then increased. The inconsistency might be due to the different deformation modes. From numerical observations from moment iii in Fig. 14, it is evident that sites A and B underwent bending deformation, resulting in a load drop in the simulated results. In the experimental results, on the other hand, severe localised deformation at C could be observed, which, unfortunately, was not predicted by the numerical model, as shown in the contours at instant iii of Fig. 14. However, further bending at A was captured by the proposed numerical model. Also, damage was found to be initiated at D_1, as highlighted in Fig. 14a, which was triggered by the shear deformation and will be further discussed in Section 4.4.

In Stage IV, the experimental force slightly decreased with increasing compression due to further bending of the folds, which was captured by the numerical model in the early stage, followed by a slight load increase due to compaction at E (the region situated above the grooves). Damage at D_1 further developed, gradually forming an oblique downward shear band, as revealed at instant iv of Fig. 14. Interestingly, the internal surface presented both downward and upward crack initiations (see D_2 in Fig. 14a) around the pre-existing rectangular groove. The upward crack was caused by the high stress triaxiality tension due to bending. The downward crack was caused by shear, similar to crack at D_1. In addition, the shear damage at D_3 was initiated. Fracture mechanisms at D_2 and D_3 will be further analysed in Section 4.4.
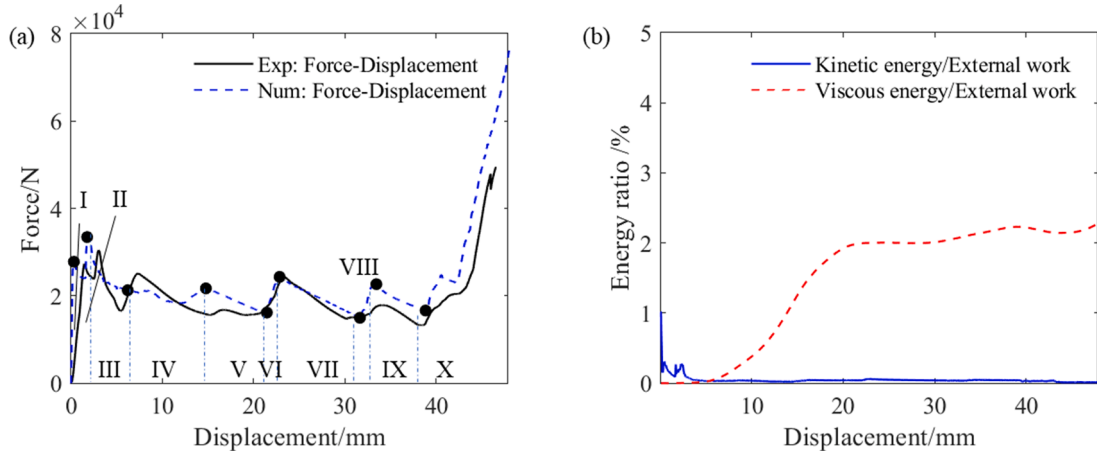
Fig. 13. Crushing responses of the axial compression specimen of 316L tubes: (a) force versus displacement curves; (b) ratio of kinetic and viscous energies to the external work versus the displacement curves. Global response in each stage was accurately predicted albeit with complicated fluctuations. Kinetic and viscous energy were negligible compared to external work, indicating the simulation was reliable for quasi-static analysis.

In stage V, the simulated loading reduced while the experimental counterpart almost remained constant. This prediction error might be caused by the error in the last stage. The final displacement and force in this stage were in good consistency with the experimental data. Also, the predicted fold deformation agreed well with the experimental results, as shown at instant v of Fig. 14, then the damage was further developed at D_1, D_2, and D_3.

In stage VI, both experimental and simulated global force increased at a high rate due to the self-contact of the tube, as shown at instant vi of Fig. 14, until formation of the next fold. Cracks further propagated around damage sites D_1, D_2, and D_3 at a higher rate than the last stage due to more severely localised deformation around the cracks. This stage was perfectly predicted by the proposed model in terms of the force-displacement response. The relative error for the both displacement and load was less than 3% throughout this stage.

In Stage VII, a gradual load drop was observed in the numerical simulation due to the combination of bending and damage evolution, which bears good agreement with the experimental data. In numerical modelling, the dropping slope was almost the same as that in Stage VI due to formation of a similar bending fold. Further, damage initiated at D_4 and D_5 were subsequently attributed to the shear stress state. Note that a fold was formed at F in both the numerical and experimental results. Overall, the predicted global response agreed very well with the experimental data.

Stages VIII and IX were very similar to Stages VI and VII, respectively. Because of the self-contact, as shown from instants viii to ix in Fig. 14, in both modelling and experiment, the global force increased first, and followed by a gradual drop due to further bending. Towards the end, both the simulated and experimental forces increased sharply owing to densification.

In summary, the phase field based numerical models exhibited high accuracy to predict the axial compression for the 316L steel tube in terms of global force-displacement response and crushing deformation. In the experiment, the tube was observed to present an asymmetric deformation mode, which was successfully captured by the numerical simulation, as shown in the deformed damage and undeformed equivalent plastic strain contours in Fig. 14. Moreover, the stress states at the instants of crack initiations were discussed and will be further analysed in Section 4.4.

4.3. Crushing behaviour of Ti-6Al-4V titanium tube

To compare the crushing behaviour of different materials, three-point bending for the Ti-6Al-4V titanium tube was also simulated. For facilitating comparison, the geometry of the specimen and loading conditions remained to be the same as the 316L steel tube, as shown in Fig. 7. Fig. 15 presents the force versus displacement curves for the Ti-6Al-4V titanium tube subject to three-point bending. Overall, it can be seen that the experimental responses were properly reproduced by the explicit phase field model. Compared with the external work, kinetic and viscous energies were negligible to ensure the quasi-static loading and physically reasonable modelling.

In Stage I, the experimental load increased nearly linearly until the peak. The predicted peak load was 13% lower than its experimental counterpart, which might be caused by the lower hardening curve. However, referring to material specimens, there is no sound justification to adjust the hardening curve. From the experimental deformation, the local indentation was observed underneath the top indenter, which was successfully captured by the numerical model, as shown at instant i of Fig. 16.

In Stage II, the experimental results indicated the presence of a shear-dominant crack around the holes, correctly captured by the proposed explicit phase field model (refer to instant ii of Fig. 16). Concurrently, the numerical results revealed that the inner surface of the indented wall experienced tensile loading, while the outer surface underwent compressive loading. The compressive damage was suppressed by the cut-off value in the Bao-Wierzbicki model, and the initiation of damage under tensile loading will be further analysed in Section 4.4.

In Stage III, the shear crack further developed in both the experimental and numerical results. The predicted crack at the top right corner around the hole agreed well with the experimental data in terms of cracking direction. At the top left corner of the hole, the experimental results showed a severe shear-induced crack, which led to a sudden loading drop and was followed by a horizontal tension-dominated crack. Such a phenomenon can also be observed in the numerical results, as presented at instant iii of Fig. 16. Also, the simulated global force-displacement responses were well correlated with the experimental data at the end of this stage.

In Stage IV, both the numerical and experimental results exhibited pronounced crack branching around the top left corner of the hole, as depicted at instant iv of Fig. 16. The presence of the vertical crack was induced by the shear loading, while the horizontal crack was indicative of tensile loading, which will be further analysed in Section 4.4. On the top right corner of the hole, however, only shear crack could be observed in the experiment. Nonetheless, the predicted global response exhibited fairly good agreement with the experimental data, as demonstrated in Fig. 16.

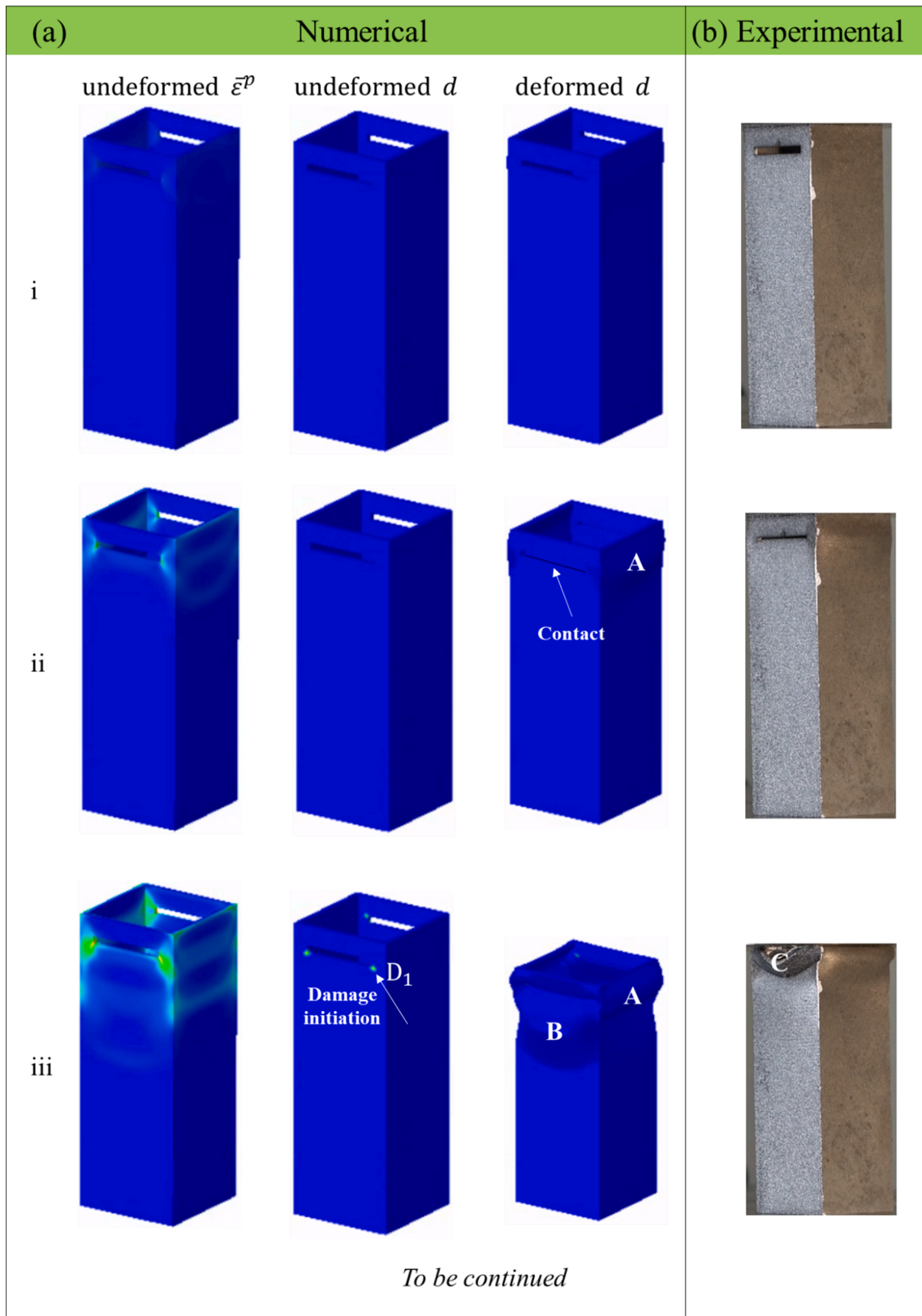In Stage V, the crack branching was further developed. Moreover,

Fig. 14. Crushing deformation of the 316L steel tube under the axial compression. (a) numerical results of undeformed equivalent plastic strain, undeformed phase field and deformed phase field; (b) experimental results. The Roman lowercase numerals i-ix denote the ends of the corresponding stages represented by the uppercase indices I-IX in Fig. 13a. The deformation mode was properly captured by the numerical model.
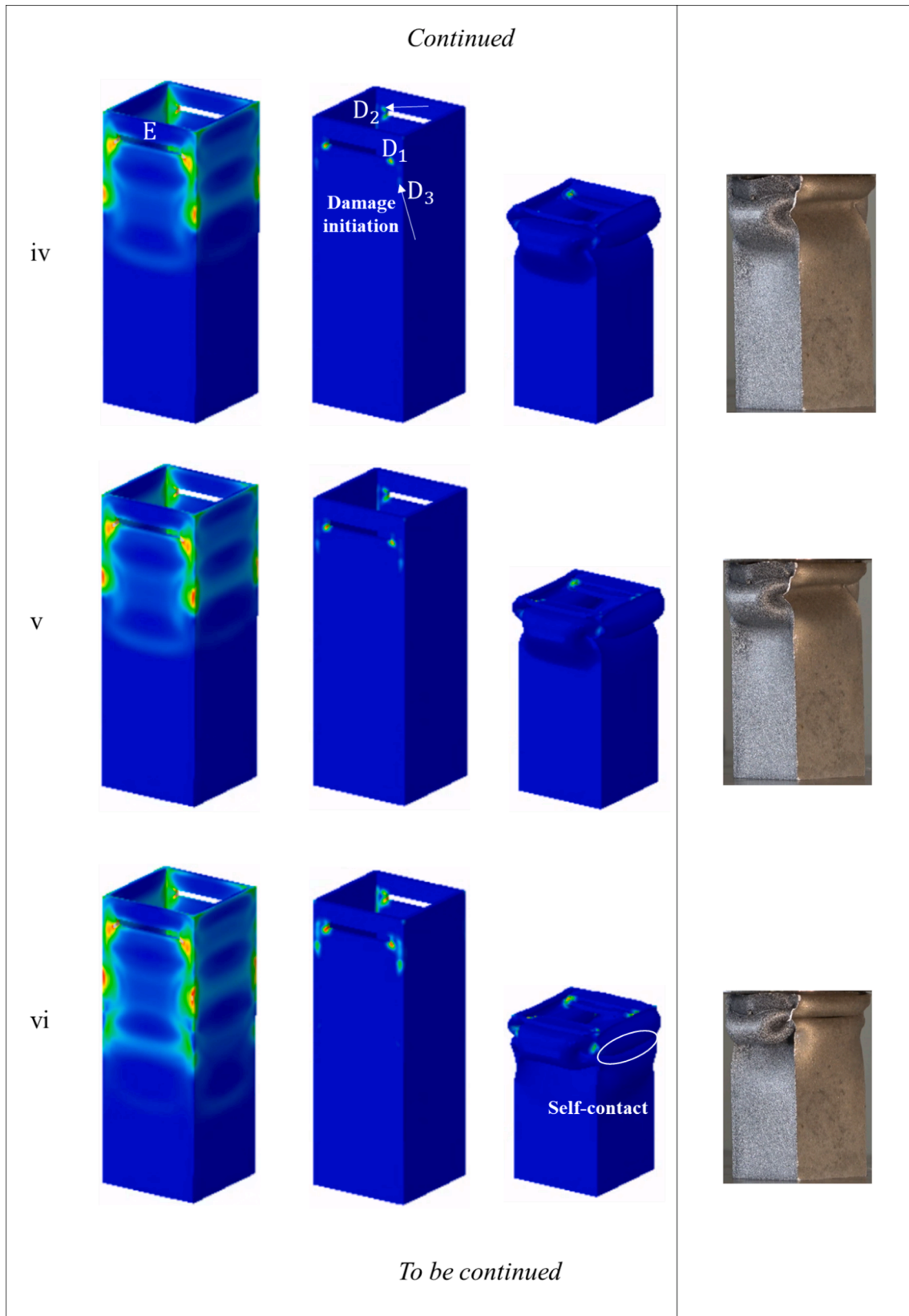
Fig. 14. (*continued*).

tension-induced cracking was observed on the top surface beneath the indenter. Overall, the explicit phase field model demonstrated its effectiveness to replicate the experimental results. Nevertheless, there are still some complex issues for future research. For example, the unsymmetrical nature of the experimental cracks may be attributed to marginal loading errors and material imperfections. Addressing uncertainties in numerical modelling [76–78] would be valuable, though it is beyond the scope of this study.
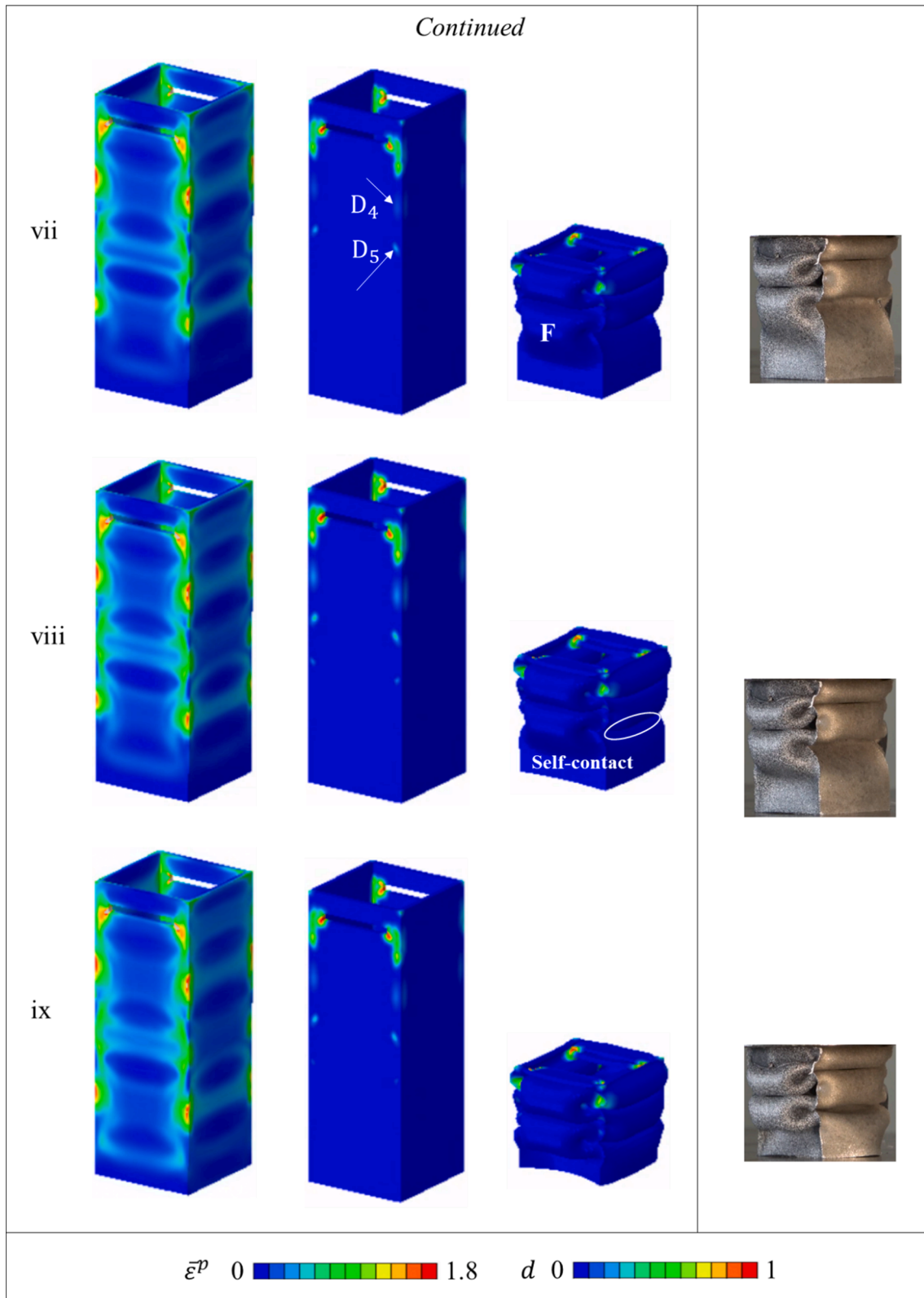
Fig. 14. (*continued*).

4.4. Further discussion on the fracture mechanisms

4.4.1. Three-point bending

To elucidate the fracture mechanism of the Ti-6Al-4V titanium tube, Fig. 17 illustrates the stress triaxiality histogram, fracture locus, damage indicator and phase field contours. According to Fig. 17a, it is evident that the most fracture was initiated under medium stress triaxiality tension, followed by shear and compression-shear induced damage initiations (see Section 2.3 for their definitions), which agrees well with the discussion on tension and shear-induced cracks in Section 4.3.
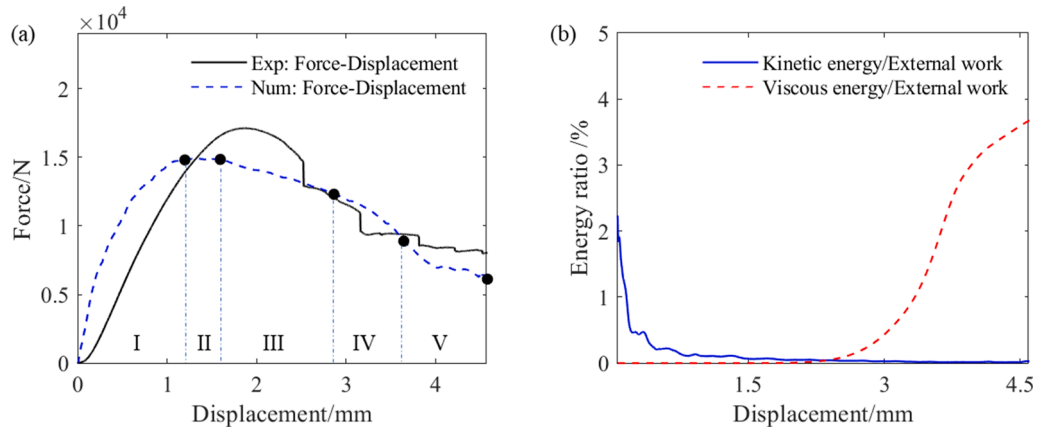
Fig. 15. Crushing responses of the three-point bending of Ti-6Al-4V tube. (a) force and versus displacement curves; (b) ratios of kinetic and viscous energies to external work versus displacement curves. The overall trend of experimental force-displacement response was fairly captured by numerical model. Kinetic and viscous energy were negligible compared to external work, indicating the simulation was reliable for quasi-static analysis.
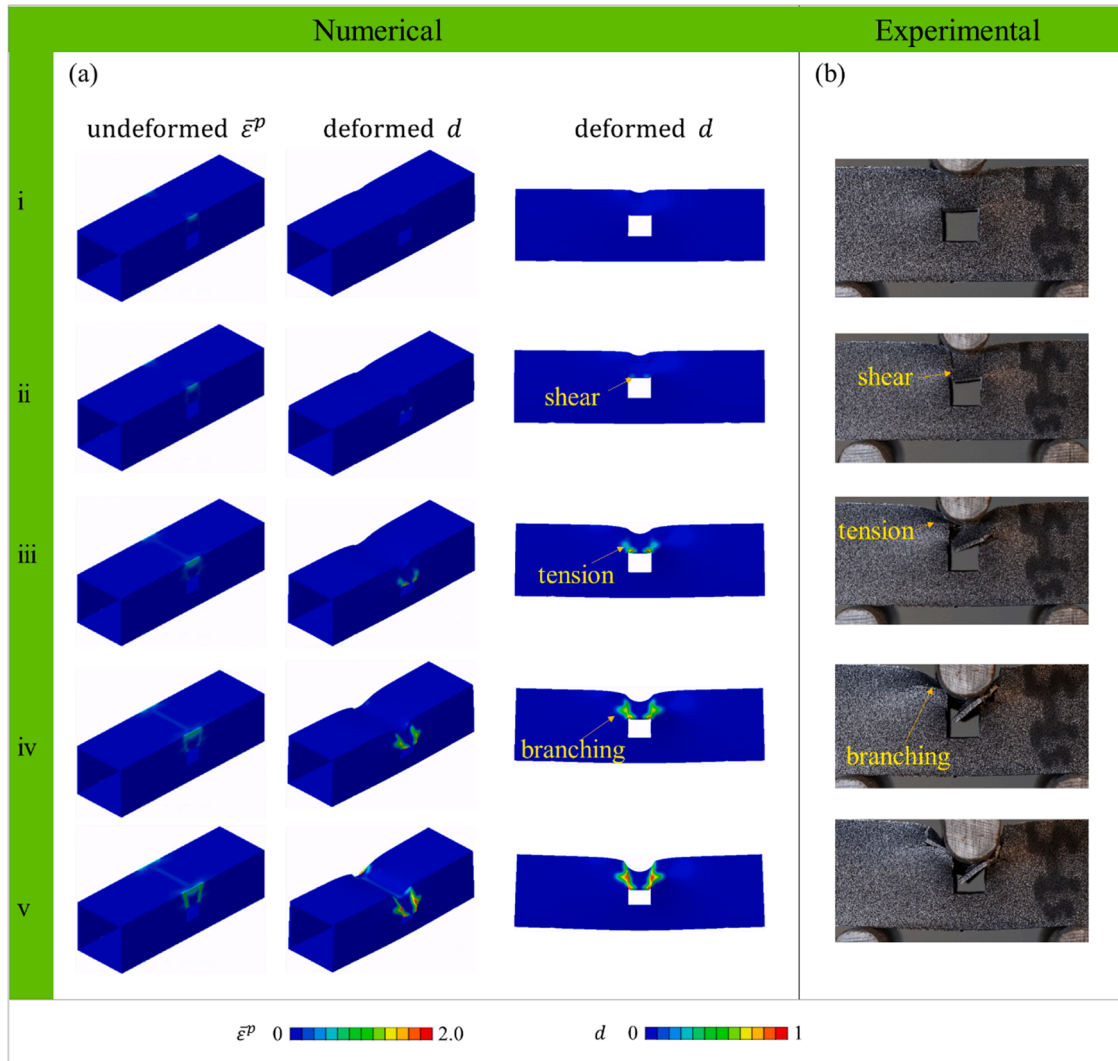

Fig. 16. Numerical and experimental results for the three-points bending tubal specimens printed by Ti-6Al-4V titanium. (a) numerical undeformed equivalent plastic strain and deformed damage contours including isometric and front view; (b) experimental deformation. The Roman lowercase numerals i-v denote the ends of the corresponding stages represented by the uppercase indices I-V in Fig. 15. The numerical model reproduced the global deformations and crack propagations.
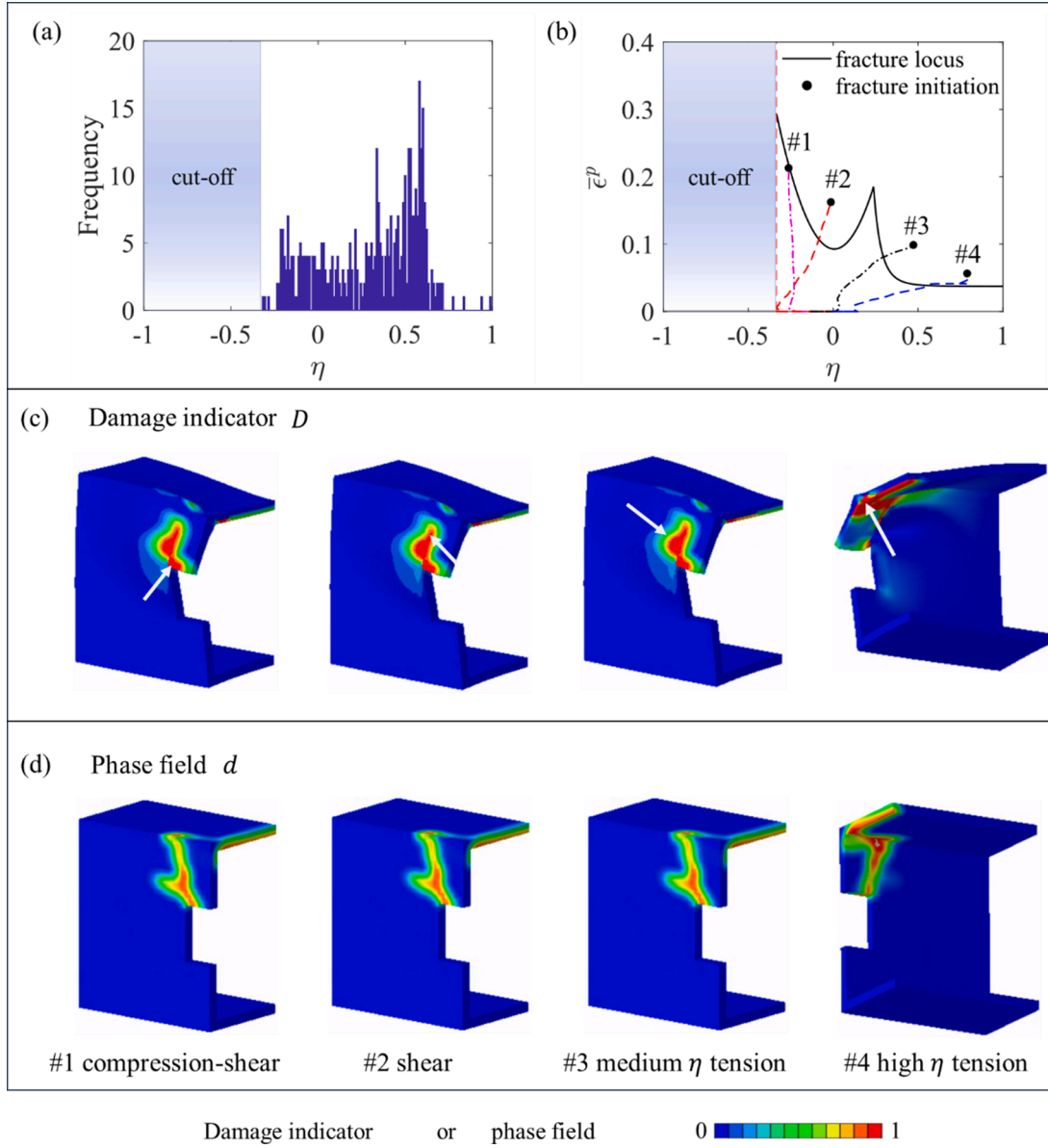
Fig. 17. Numerical results of simulated three-point bending of the Ti-6Al-4V tube. (a) histogram of the stress triaxiality at the instant of damage initiation, i.e., $D = 1$ as defined in Eq. (15); (b) fracture locus and loading history of typical material points with their locations highlighted in (c). (c-e) numerical contours of damage indicator and phase field damage of representative material points selected in (b). ¼ model was used to provide detailed visualisation of internal structural deformation. Notably, due to the non-proportional loading history, the fracture initiation points #2 and #3 deviated significantly from the fracture locus. Furthermore, while cracks were induced by a broad range of stress states, they were primarily caused by tension with medium stress triaxiality and shear loading.

Fig. 17b illustrates the fracture locus of the calibrated Bao-Wierzbicki model, along with the loading histories of the representative elements. These elements were subjected to compression-shear, shear, and medium and high stress triaxiality tension, respectively, at the instant of fracture initiation. The loading histories were considerably complicated and will be discussed later. Also, it is worth noting that the fracture initiation points #2, #3 and #4 did not precisely locate on the fracture locus due to non-proportional loading [52], as discussed in Section 2.4.

At crack #1, which was located at the top left corner of the square hole (Fig. 17c), was initiated from compression-shear loading. It is noted that the stress state remained relatively stable without significant change in stress triaxiality involving the equivalent plastic strain. It could be regarded as a proportional loading (see Section 2.4), resulting in the fracture initiation point located on the fracture locus. The element underwent complete rupture as a result of extensive plastic deformation,

as depicted in the first subplot of Fig. 17d.

At cracks #2, #3, and #4, strong non-proportionality of loading could be observed. Crack #2 and crack #3 were observed to locate on the two branches of the branched cracks, respectively, as shown in the second and third subplots in Fig. 17c. Crack #2 started with compressive loading and then transitioned to the shear region, whereas crack #3 initiated from shear and transitioned to tension loading. Therefore, their equivalent plastic strains at the instant of fracture initiation were much larger than the corresponding fracture strains due to non-proportional loading. Crack #4, situated on the inner surface of the tube, experienced a complex loading history, starting with compression, transitioning to shear, followed by tension under intermediate stress triaxiality, and ending with tension under high stress triaxiality. Due to its rapid change in stress triaxiality, its equivalent plastic strains at the instant of fracture initiation were also larger than the corresponding fracture strain.
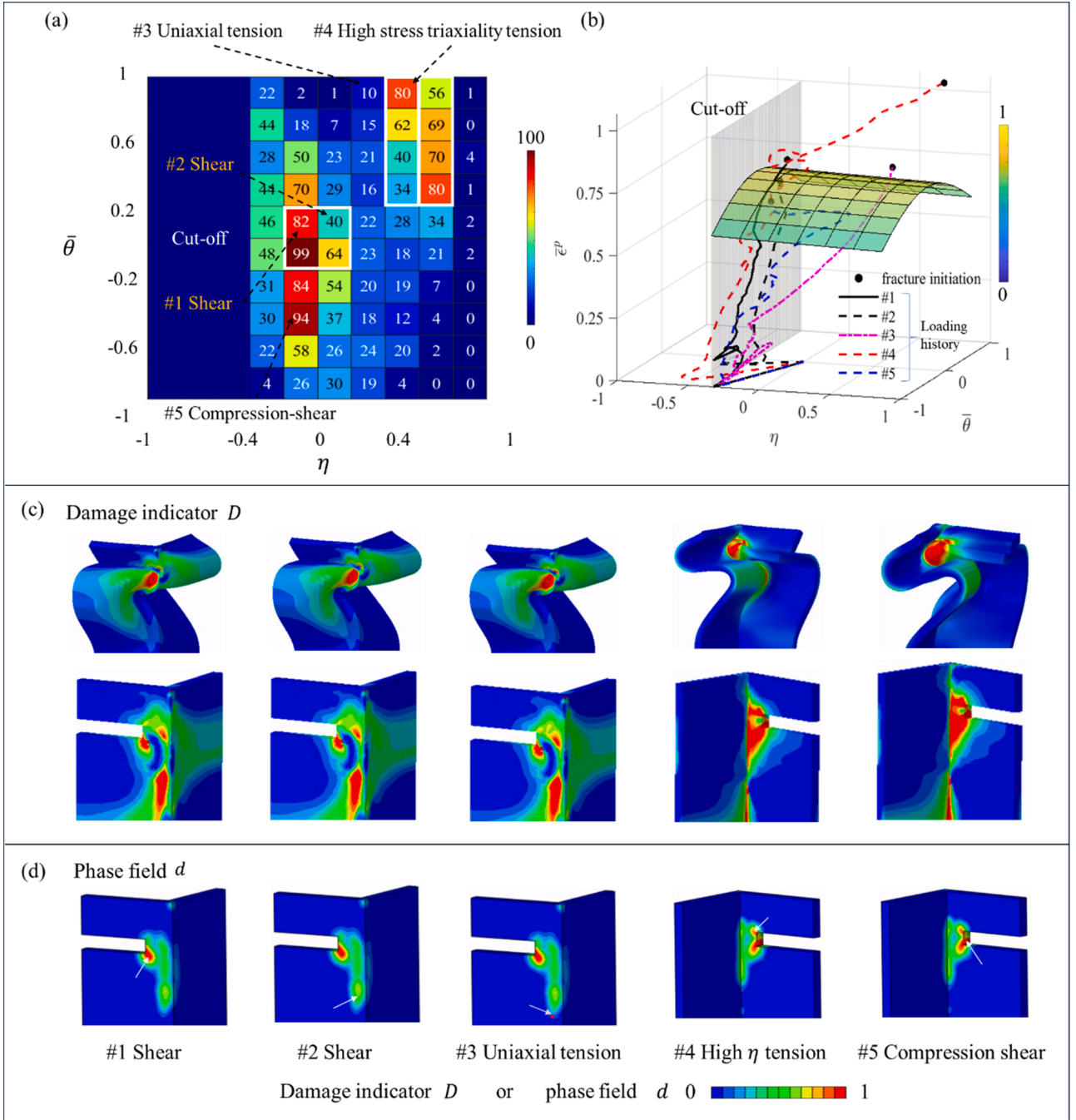
Fig. 18. Numerical modelling results of axial compression of the 316L tube. (a) Heatmap of the stress state at the instant of damage initiation, i.e., $D = 1$ as defined in Eq. (15). Numbers indicate the numbers of elements falling within the stress state ranges; (b) Fracture envelope and loading histories of representative material points highlighted in (d); (c) contours of damage indicator, and (d) contours of phase field damage in selected elements in (a).

In the case of three-point bending of the Ti-6Al-4V tube, tension-induced damage appeared to be more pronounced, primarily attributed to the lower fracture strain and larger tensile zone. However, the shear-induced crack seemed to cause more destructive damage to the tube structure. Only following the development of the vertical shear crack, did the side wall start bending outwards, resulting in the formation of the horizontal tensile cracks, as presented in Fig. 16. Furthermore, the global crushing force exhibited a continuous decrease following the initiation of shear cracks. In contrast, in the case of the 316L steel tube, no shear crack was observed, contributing to a significantly delayed reduction in global crushing force.

4.4.2. Axial compression

Fig. 18a displays the stress state heatmap for all the elements in the axial compression model of the 316L steel tube at the instant of crack initiation. The heatmap reveals the stress states can include shear, medium and high stress triaxiality tension, as well as compression-shear. To further investigate the fracture mechanism under the axial compression, Fig. 18b shows five selected material points together with their loading histories and fracture envelope. Cracks #1, #2, and #3 were situated on the outer surface of the tube, while cracks #4 and #5 were positioned on the inner surface.

Cracks labelled #1 and #2 were observed at the bottom corner of the rectangular groove and the edge of the square tube, respectively, as

highlighted in Fig. 18c and d. Based on their loading histories (see Fig. 18b), the stress states initially underwent compression but gradually transitioned towards shear. Non-proportional loadings were apparent initially but were diminished when $\bar{\varepsilon}^p$ exceeded 0.1, unveiling that the fracture initiation points were positioned marginally above the fracture envelope. Further, it was found that crack #2 exhibited more rigid body rotation and less plastic deformation, whereas crack #1 showed the opposite behaviour, as depicted in Fig. 18d. This situation resulted in some distinct crack evolutions where crack #1 fully developed while the maximum phase field value for crack #2 could only reach 0.5 approximately.

Prior to the fracture initiation, the stress states of crack #3, despite its proximity to crack #2, were notably different. Initially, crack #3 experienced compression, followed by shear, and eventually reached a state of uniaxial tension, as illustrated in Fig. 18b. It is noted that the stress states changed remarkably throughout the loading process, leading to a much greater $\bar{\varepsilon}^p$ than the corresponding fracture strain at the instant of fracture initiation. Nevertheless, the development of crack #3 remained incomplete, resembling that of crack #2 due to its limited plastic deformation after fracture initiation.

Crack #4, located at the top corner of the groove on the internal surface, as shown in Fig. 18c and e, initially experienced compression, resulting in substantial deformation confined to the cut-off region, which did not contribute to the accumulation of damage indicator *D*. Subsequently, the tearing deformation of its upper and lower folds led to shear and tension states with varying levels of stress triaxiality, ranging from low to medium and high. The highly non-proportional loading history explained the significantly higher fracture initiation point in Fig. 18b compared to the fracture envelope.

Crack #5, situated at the bottom corner of the groove on the internal surface (Fig. 18c), started with compression-shear and then transitioned to shear. Although it fluctuated into the low stress triaxiality tension region, it soon returned to compression-shear loading due to the squeezing deformation. Note that tension accelerated the accumulation of damage indicators in the model, whereas shear and compression exhibited a contrasting trend due to the lower fracture strain under tension (see Fig. 4). Ultimately, both crack #4 and crack #5 fully developed due to significant plastic deformation.

In summary, non-proportional loading played a significant role in the crushing behaviour of both materials and loading conditions. Unlike material samples under simple loading conditions, where the stress states remained relatively stable throughout the loading history [79,80], crushing a sophisticated structure could experience considerable variations in stress states at material points, potentially resulting in fracture initiation points away from the fracture locus. If only proportional loadings were considered in such cases, non-physical fracture initiation could occur in numerical simulations. Hence, it is essential to consider non-proportional loading within the phase field framework to correctly predict crushing behaviour.

5. Conclusions

This study presents a novel explicit phase field model for predicting the crushing behaviour of additively manufactured metallic structures. The model was formulated in line with a variational principle and then enhanced by incorporating fracture criteria for ductile fracture with non-proportional loading histories. Plastic behaviour was captured using the transversely isotropic Hill48 model. Fracture initiation was predicted using the modified Mohr-Coulomb model for LPBF 316L and the Bao-Wierzbicki model for Ti-6Al-4V. During the crushing process of additively manufactured structures, the stress state of material points can vary significantly with the loading. Therefore, the history of non-proportional loading is incorporated into the phase field model in this

work. The proposed phase field model was implemented numerically using the ABAQUS/Explicit solver via user-defined subroutines.

Five material specimens with LPBF 316L steel and Ti-6Al-4V titanium were designed, fabricated and tested to calibrate the proposed model. From the force-displacement curves, it can be found that the calibrated model was acceptable in terms of elastoplastic responses and fracture behaviour. Then, the square tubes were printed and tested under three-point bending and axial compression, respectively. The modelling results revealed that the crushing behaviour of both additively manufactured structures could be properly reproduced in terms of force-displacement curves and crack paths.

More importantly, the fracture mechanism was analysed through experimental tests and numerical modelling. For the three-point bending of Ti-6Al-4V titanium tubes, cracks were mainly induced by the medium stress triaxiality tension and shear loading. For the axial compression of the 316L steel tubes, the stress states of critical elements were relatively diverse yet slightly concentrated in terms of the shear, compression-shear, and high stress triaxiality tension. Remarkably, non-proportional loading is significant in crushing deformation as a material point may experience varying stress states. Without considering non-proportional loading, it may lead to non-physical predictions.

In summary, this work contributes an explicit phase field model for simulating crushing behaviour of additively manufactured metals, which has been validated by extensive experimental tests. Note that while the framework is proposed for 3D printed metals, it applies to general metallic materials. However, phase field approaches necessitate local refinement of elements within the damaged area to simulate localised cracks, which requires high computational cost. This might be addressed by adaptive meshing techniques [81,82] such that mesh can be refined and/or coarsened based on user defined criteria to improve the accuracy and efficiency. Furthermore, the impact of the 3D printing process [83] and heat treatment [84] on mechanical behaviour remains unexplored, highlighting the need for further investigations.

CRediT authorship contribution statement

Cunyi Li: Data curation, Formal analysis, Investigation, Methodology, Writing – original draft. **Jianguang Fang:** Conceptualization, Funding acquisition, Methodology, Project administration, Resources, Supervision, Writing – review & editing. **Na Qiu:** Investigation, Resources. **Chi Wu:** Methodology, Writing – original draft. **Grant Steven:** Funding acquisition, Methodology, Supervision, Writing – review & editing. **Qing Li:** Funding acquisition, Methodology, Supervision, Writing – review & editing.

Declaration of competing interest

The authors declare that they have no known competing financial interests or personal relationships that could have appeared to influence the work reported in this paper.

Data availability

Data will be made available on request.

Acknowledgments

Appendix

A1. Strain hardening curves

The strain hardening curves of both 316L steel and Ti-6Al-4V titanium are presented in Fig. A1. Before necking, the hardening curves were determined from 90° UT specimen. After necking, the hardening curves were determined via inverse identification [85,86] to minimise the predicting error of the force-displacement curves for all material samples.
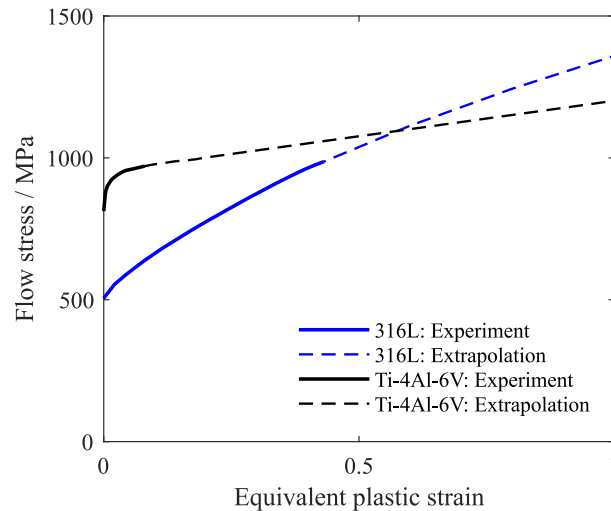

Fig. A1. Strain hardening curves of additively manufactured 316L steel [50] and Ti-6Al-4V titanium. Hardening curves were extrapolated for the post-necking stage to match experimental force-displacement curves for all material specimens.

References

[1] Wu JY, Nguyen VP, Nguyen CT, Sutula D, Sinaie S, Bordas SP. Phase-field modeling of fracture. Adv Appl Mech 2020;53:1–183.

[2] Francfort GA, Marigo JJ. Revisiting brittle fracture as an energy minimization problem. J Mech Phys Solids 1998;46(8):1319–42.

[3] Bourdin B, Francfort GA, Marigo JJ. Numerical experiments in revisited brittle fracture. J Mech Phys Solids 2000;48(4):797–826.

[4] Ambati M, Gerasimov T, De Lorenzis L. A review on phase-field models of brittle fracture and a new fast hybrid formulation. Comput Mech 2014;55(2):383–405.

[5] Wu JY, Nguyen VP. A length scale insensitive phase-field damage model for brittle fracture. J Mech Phys Solids 2018;119:20–42.

[6] Ambati M, Gerasimov T, De Lorenzis L. Phase-field modeling of ductile fracture. Comput Mech 2015;55(5):1017–40.

[7] Miehe C, Aldakheel F, Raina A. Phase field modeling of ductile fracture at finite strains: a variational gradient-extended plasticity-damage theory. Int J Plast 2016; 84:1–32.

[8] Borden MJ, Verhoosel CV, Scott MA, Hughes TJ, Landis CM. A phase-field description of dynamic brittle fracture. Comput Methods Appl Mech Eng 2012;217: 77–95.

[9] Chu D, Li X, Liu Z, Cheng J, Wang T, Li Z, Zhuang Z. A unified phase field damage model for modeling the brittle-ductile dynamic failure mode transition in metals. Eng Fract Mech 2019;212:197–209.

[10] Feng Y, Wu D, Stewart MG, Gao W. Past, current and future trends and challenges in non-deterministic fracture mechanics: a review. Comput Methods Appl Mech Eng 2023;412:116102.

[11] Gerasimov T, Römer U, Vondřejc J, Matthies HG, De Lorenzis L. Stochastic phase-field modeling of brittle fracture: computing multiple crack patterns and their probabilities. Comput Methods Appl Mech Eng 2020;372:113353.

[12] Miehe C, Hofacker M, Schänzel LM, Aldakheel F. Phase field modeling of fracture in multi-physics problems. Part II. Coupled brittle-to-ductile failure criteria and crack propagation in thermo-elastic–plastic solids. Comput Methods Appl Mech Eng 2015;294:486–522.

[13] Dittmann M, Aldakheel F, Schulte J, Schmidt F, Krüger M, Wriggers P, et al. Phase-field modeling of porous-ductile fracture in non-linear thermo-elasto-plastic solids. Comput Methods Appl Mech Eng 2020;361:112730.

[14] Zhang J, Lu G, You Z. Large deformation and energy absorption of additively manufactured auxetic materials and structures: a review. Compos Part B Eng 2020; 201:108340.

[15] Wu Y, Fang J, Wu C, Li C, Sun G, Li Q. Additively manufactured materials and structures: a state-of-the-art review on their mechanical characteristics and energy absorption. Int J Mech Sci 2023;108102.

[16] Langseth M, Hopperstad O. Static and dynamic axial crushing of square thin-walled aluminium extrusions. Int J Impact Eng 1996;18(7-8):949–68.

[17] Tran T, Le D, Baroutaji A. Theoretical and numerical crush analysis of multi-stage nested aluminium alloy tubular structures under axial impact loading. Eng Struct 2019;182:39–50.

[18] Sato K, Inazumi T, Yoshitake A, Liu SD. Effect of material properties of advanced high strength steels on bending crash performance of hat-shaped structure. Int J Impact Eng 2013;54:1–10.

[19] Liu W, Lian J, Münstermann S, Zeng C, Fang X. Prediction of crack formation in the progressive folding of square tubes during dynamic axial crushing. Int J Mech Sci 2020;176:105534.

[20] Giglio M, Manes A, Viganò F. Ductile fracture locus of Ti–6Al–4V titanium alloy. Int J Mech Sci 2012;54(1):121–35.

[21] Li X, Roth CC, Tancogne-Dejean T, Mohr D. Rate-and temperature-dependent plasticity of additively manufactured stainless steel 316L: characterization, modeling and application to crushing of shell-lattices. Int J Impact Eng 2020;145: 103671.

[22] Qiu N, Zhang J, Li C, Shen Y, Fang J. Mechanical properties of three-dimensional functionally graded triply periodic minimum surface structures. Int J Mech Sci 2023;246:108118.

[23] Mohr D, Marcadet SJ. Micromechanically-motivated phenomenological Hosford–Coulomb model for predicting ductile fracture initiation at low stress triaxialities. Int J Solids Struct 2015;67-68:40–55.

[24] Bao Y, Wierzbicki T. On fracture locus in the equivalent strain and stress triaxiality space. Int J Mech Sci 2004;46(1):81–98.

[25] Andrade FXC, Feucht M, Haufe A, Neukamm F. An incremental stress state dependent damage model for ductile failure prediction. Int J Fract 2016;200(1-2): 127–50.

[26] Pijaudier-Cabot G, Bažant ZP, Tabbara M. Comparison of various models for strain-softening. Eng Comput 1988;5(2):141–50.

[27] Needleman A. Material rate dependence and mesh sensitivity in localization problems. Comput Methods Appl Mech Eng 1988;67(1):69–85.

[28] Areias P, Rabczuk T, Msekh MA. Phase-field analysis of finite-strain plates and shells including element subdivision. Comput Methods Appl Mech Eng 2016;312: 322–50.

[29] de Borst R, Verhoosel CV. Gradient damage vs phase-field approaches for fracture: Similarities and differences. Comput Methods Appl Mech Eng 2016;312:78–94.

[30] Peerlings RH, de Borst R, Brekelmans WM, de Vree J. Gradient enhanced damage for quasi-brittle materials. Int J Numer Methods Eng 1996;39(19):3391–403.

[31] Prior A. Applications of implicit and explicit finite element techniques to metal forming. J Mater Process Technol 1994;45(1-4):649–56.

[32] Sun J, Lee K, Lee H. Comparison of implicit and explicit finite element methods for dynamic problems. J Mater Process Technol 2000;105(1-2):110–8.

[33] Santosa SP, Wierzbicki T, Hanssen AG, Langseth M. Experimental and numerical studies of foam-filled sections. Int J Impact Eng 2000;24(5):509–34.

[34] Ahmad Z, Thambiratnam D. Crushing response of foam-filled conical tubes under quasi-static axial loading. Mater Des 2009;30(7):2393–403.

[35] Ren HL, Zhuang XY, Anitescu C, Rabczuk T. An explicit phase field method for brittle dynamic fracture. Comput Struct 2019;217:45–56.

[36] Ziaei-Rad V, Shen Y. Massive parallelization of the phase field formulation for crack propagation with time adaptivity. Comput Methods Appl Mech Eng 2016; 312:224–53.

[37] Mandal TK, Nguyen VP, Wu JY. A length scale insensitive anisotropic phase field fracture model for hyperelastic composites. Int J Mech Sci 2020;188:105941.

[38] Zhang Z, Qiu Y, Hu Z, Ye H, Zhang H, Zheng Y. Explicit phase-field total Lagrangian material point method for the dynamic fracture of hyperelastic materials. Comput Methods Appl Mech Eng 2022;398:115234.

[39] Wenlong Zhang AT. An efficient implementation of phase field method with explicit time integration. J Appl Comput Mech 2020;6(3):373–82.

[40] Wang T, Ye X, Liu Z, Liu X, Chu D, Zhuang Z. A phase-field model of thermo-elastic coupled brittle fracture with explicit time integration. Comput Mech 2020;65(5): 1305–21.

[41] Hu X, Tan S, Xia D, Min L, Xu H, Yao W, et al. An overview of implicit and explicit phase field models for quasi-static failure processes, implementation and computational efficiency. Theor Appl Fract Mech 2023;124:103779.

[42] Sahin U, Ren H, Imrak CE, Rabczuk T. Computational modeling of quasi static fracture using the nonlocal operator method and explicit phase field model. Eng Comput 2023:1–12.

[43] Wang T, Liu ZL, Cui YN, Ye X, Liu XM, Tian R, et al. A thermo-elastic-plastic phase-field model for simulating the evolution and transition of adiabatic shear band. Part I. Theory and model calibration. Eng Fract Mech 2020;232:107028.

[44] Wang T, Liu ZL, Cui YN, Ye X, Liu XM, Tian R, et al. A thermo-elastic-plastic phase-field model for simulating the evolution and transition of adiabatic shear band. Part II. Dynamic collapse of thick-walled cylinder. Eng Fract Mech 2020;231: 107027.

[45] Hu Z, Liu Y, Zhang Z, Ye H, Zhang H, Zheng Y. Coupling explicit phase-field MPM for two-dimensional hydromechanical fracture in poro-elastoplastic media. Int J Mech Sci 2023;260:108649.

[46] Borden MJ, Hughes TJR, Landis CM, Anvari A, Lee IJ. A phase-field formulation for fracture in ductile materials: finite deformation balance law derivation, plastic degradation, and stress triaxiality effects. Comput Methods Appl Mech Eng 2016; 312:130–66.

[47] Huber W, Asle Zaeem M. A mixed mode phase-field model of ductile fracture. J Mech Phys Solids 2023;171:105123.

[48] Li C, Fang J, Wu C, Sun G, Steven G, Li Q. Phase field fracture in elasto-plastic solids: incorporating phenomenological failure criteria for ductile materials. Comput Methods Appl Mech Eng 2022;391:114580.

[49] Abrari Vajari S, Neuner M, Arunachala PK, Ziccarelli A, Deierlein G, Linder C. A thermodynamically consistent finite strain phase field approach to ductile fracture considering multi-axial stress states. Comput Methods Appl Mech Eng 2022;400:115467.

[50] Li C, Fang J, Wan Y, Qiu N, Steven G, Li Q. Phase field fracture model for additively manufactured metallic materials. Int J Mech Sci 2023;251:108324.

[51] Bai Y, Wierzbicki T. A new model of metal plasticity and fracture with pressure and lode dependence. Int J Plast 2008;24(6):1071–96.

[52] Papasidero J, Doquet V, Mohr D. Ductile fracture of aluminum 2024-T351 under proportional and non-proportional multi-axial loading: Bao–Wierzbicki results revisited. Int J Solids Struct 2015;69-70:459–74.

[53] Zhuang X, Wang T, Zhu X, Zhao Z. Calibration and application of ductile fracture criterion under non-proportional loading condition. Eng Fract Mech 2016;165: 39–56.

[54] Benzerga AA, Surovik D, Keralavarma SM. On the path-dependence of the fracture locus in ductile materials – analysis. Int J Plast 2012;37:157–70.

[55] Hong S, Pan J, Tyan T, Prasad P. Quasi-static crush behavior of aluminum honeycomb specimens under non-proportional compression-dominant combined loads. Int J Plast 2006;22(6):1062–88.

[56] Alessi R, Ambati M, Gerasimov T, Vidoli S, De Lorenzis L. Comparison of phase-field models of fracture coupled with plasticity. Advances in computational plasticity 2018:1–21.

[57] Miehe C, Welschinger F, Hofacker M. Thermodynamically consistent phase-field models of fracture: variational principles and multi-field FE implementations. Int J Numer Methods Eng 2010;83(10):1273–311.

[58] Belytschko T, Liu WK, Moran B, Elkhodary K. Nonlinear finite elements for continua and structures. John Wiley & Sons ltd; 2014.

[59] Brepols T, Vladimirov IN, Reese S. Numerical comparison of isotropic hypo- and hyperelastic-based plasticity models with application to industrial forming processes. Int J Plast 2014;63:18–48.

[60] Wilson-Heid AE, Qin S, Beese AM. Multiaxial plasticity and fracture behavior of stainless steel 316L by laser powder bed fusion: Experiments and computational modeling. Acta Mater 2020;199:578–92.

[61] Qin S, Wang Z, Beese AM. Orientation and stress state dependent plasticity and damage initiation behavior of stainless steel 304L manufactured by laser powder bed fusion additive manufacturing. Extrem Mech Lett 2021;45:101271.

[62] Jackiewicz J. Use of a modified Gurson model approach for the simulation of ductile fracture by growth and coalescence of microvoids under low, medium and high stress triaxiality loadings. Eng Fract Mech 2011;78(3):487–502.

[63] Kang L, Ge H, Fang X. An improved ductile fracture model for structural steels considering effect of high stress triaxiality. Constr Build Mater 2016;115:634–50.

[64] Peng Z, Zhao H, Li X. New ductile fracture model for fracture prediction ranging from negative to high stress triaxiality. Int J Plast 2021;145:103057.

[65] Bai Y, Wierzbicki T. Application of extended Mohr–Coulomb criterion to ductile fracture. Int J Fract 2009;161(1):1–20.

[66] Seetoh IP, Liu X, Markandan K, Zhen L, Lai CQ. Strength and energy absorption characteristics of Ti6Al4V auxetic 3D anti-tetrachiral metamaterials. Mech Mater 2021;156:103811.

[67] Abedini A, Butcher C, Worswick MJ. Experimental fracture characterisation of an anisotropic magnesium alloy sheet in proportional and non-proportional loading conditions. Int J Solids Struct 2018;144-145:1–19.

[68] Alessi R, Marigo JJ, Maurini C, Vidoli S. Coupling damage and plasticity for a phase-field regularisation of brittle, cohesive and ductile fracture: One-dimensional examples. Int J Mech Sci 2018;149:559–76.

[69] Dean A, Reinoso J, Jha NK, Mahdi E, Rolfes R. A phase field approach for ductile fracture of short fibre reinforced composites. Theor Appl Fract Mech 2020;106: 102495.

[70] Miehe C, Hofacker M, Welschinger F. A phase field model for rate-independent crack propagation: robust algorithmic implementation based on operator splits. Comput Meth Appl Mech Eng 2010;199(45–48):2765–78.

[71] Kumar D, Jhavar S, Arya A, Prashanth KG, Suwas S. Mechanisms controlling fracture toughness of additively manufactured stainless steel 316L. Int J Fract 2021;235(1):61–78.

[72] Soltani-Tehrani A, Isaac JP, Tippur HV, Silva DF, Shao S, Shamsaei N. Ti-6Al-4V powder reuse in laser powder bed fusion (L-PBF): the effect on porosity, microstructure, and mechanical behavior. Int J Fatigue 2023;167:107343.

[73] Dittmann M, Aldakheel F, Schulte J, Wriggers P, Hesch C. Variational phase-field formulation of non-linear ductile fracture. Comput Methods Appl Mech Eng 2018; 342:71–94.

[74] Yin B, Kaliske M. A ductile phase-field model based on degrading the fracture toughness: theory and implementation at small strain. Comput Methods Appl Mech Eng 2020;366:113068.

[75] Wang T, Ye X, Liu Z, Chu D, Zhuang Z. Modeling the dynamic and quasi-static compression-shear failure of brittle materials by explicit phase field method. Comput Mech 2019;64(6):1537–56.

[76] Noii N, Khodadadian A, Ulloa J, Aldakheel F, Wick T, François S, Wriggers P. Bayesian inversion for unified ductile phase-field fracture. Comput Mech 2021;68 (4):943–80.

[77] Nagaraja S, Römer U, Matthies HG, De Lorenzis L. Deterministic and stochastic phase-field modeling of anisotropic brittle fracture. Comput Methods Appl Mech Eng 2023;408:115960.

[78] Neuner M, Vajari SA, Arunachala P, Linder C. A better understanding of the mechanics of borehole breakout utilizing a finite strain gradient-enhanced micropolar continuum model. Comput Geotech 2023;153:105064.

[79] Jia Y, Bai Y. Ductile fracture prediction for metal sheets using all-strain-based anisotropic eMMC model. Int J Mech Sci 2016;115-116:516–31.

[80] Qin S, Beese AM. Multiaxial fracture of DP600: experiments and finite element modeling. Mater Sci Eng A 2020;785:139386.

[81] Gupta A, Krishnan UM, Mandal TK, Chowdhury R, Nguyen VP. An adaptive mesh refinement algorithm for phase-field fracture models: application to brittle, cohesive, and dynamic fracture. Comput Methods Appl Mech Eng 2022;399: 115347.

[82] Hirshikesh ALNP, Annabattula RK, Ooi ET, Song C, Natarajan S. Adaptive phase-field modeling of brittle fracture using the scaled boundary finite element method. Comput Methods Appl Mech Eng 2019;355:284–307.

[83] Smith WL, Roehling JD, Strantza M, Ganeriwala RK, Ashby AS, Vrancken B, et al. Residual stress analysis of *in situ* surface layer heating effects on laser powder bed fusion of 316L stainless steel. Addit Manuf 2021;47:102252.

[84] Jiang J, Ren Z, Ma Z, Zhang T, Zhang P, Zhang DZ, et al. Mechanical properties and microstructural evolution of TA15 Ti alloy processed by selective laser melting before and after annealing. Mater Sci Eng A 2020;772:138742.

[85] Dunand M, Mohr D. Hybrid experimental–numerical analysis of basic ductile fracture experiments for sheet metals. Int J Solids Struct 2010;47(9):1130–43.

[86] Pack K, Luo M, Wierzbicki T. Sandia Fracture Challenge: blind prediction and full calibration to enhance fracture predictability. Int J Fract 2014;186(1-2):155–75.